

Surfactant protein C, a modulator of paravascular brain waste clearance, is associated with perineuronal nets and shows age-dependent changes of brain content and characteristic deposits in wildtype and 3xTg mice

Stefan Schob (✉ schob.stefan@googlemail.com)

University Hospital Halle: Universitätsklinikum Halle <https://orcid.org/0000-0003-2846-5443>

Joana Puchta

University Hospital Leipzig Institute for Neuroradiology: Universitätsklinikum Leipzig Institut für Neuroradiologie

Karsten Winter

University of Leipzig: Institute for Anatomy

Dominik Michalski

University Hospital Leipzig: Department of Neurology

Bianca Mages

University of Leipzig: Institute for Anatomy

Henrik Martens

Synaptic Systems Göttingen

Alexander Emmer

University Hospital Halle: Clinic and Policlinic of Neurology

Karl-Titus Hoffmann

University Hospital Leipzig Institute for Neuroradiology: Universitätsklinikum Leipzig Institut für Neuroradiologie

Frank Gaunitz

University Hospital Leipzig: Clinic and Policlinic of Neurosurgery

Anton Meinicke

University of Leipzig Paul Flechsig Institute for Brain Research

Matthias Krause

Universitätsklinikum Leipzig: Universitätsklinikum Leipzig

Wolfgang Härtig

University of Leipzig Paul Flechsig Institute for Brain Research

Keywords: SP-C, hippocampus, neurovascular unit, S100 β , extracellular matrix, perineuronal net, WFA, Reelin, VGLUT2, β -amyloid, hyperphosphorylated tau

Posted Date: August 11th, 2021

DOI: <https://doi.org/10.21203/rs.3.rs-747032/v1>

License:  This work is licensed under a Creative Commons Attribution 4.0 International License.

[Read Full License](#)

Abstract

Surfactant Protein C (SP-C) modulates cerebrospinal fluid (CSF) rheology. During ageing, its declining levels are accompanied by an increased burden of white matter lesions. Pulmonary SP-C intermediates harbouring the BRICHOS-domain prevent protein misfolding in the lungs. Thus, cerebral SP-C intermediates may counteract cerebral β -amyloidosis, a hallmark of Alzheimer's disease (AD). However, data on the molecular neuroanatomy of SP-C and its alterations in wildtype and triple transgenic (3xTg) mice, featuring essential elements of AD-neuropathology, are lacking. Therefore, this study investigated SP-C-containing structures in murine forebrains and their spatial relationships with vascular, glial and neuronal components of the neurovascular unit. Fluorescence labelling demonstrated neuronal SP-C in the medial habenula, the indusium griseum and the hippocampus. Glial counterstaining elucidated astrocytes in the corpus callosum co-expressing SP-C and S100 β . Notably, perineuronal nets were associated with SP-C in the nucleus reticularis thalami, the lateral hypothalamus and the retrosplenial cortex. In the hippocampus of aged 3xTg mice, an increased number of dot-like depositions containing SP-C and Reelin, but devoid of BRICHOS-immunoreactivity were observed apart from AD-like lesions. Wildtype and 3xTg mice revealed an age-dependent increase of such deposits markedly pronounced in about 24-month-old 3xTg mice. SP-C levels of the intracellular and extracellular compartments in each group revealed an inverse correlation of SP-C and Reelin, with reduced SP-C and increased Reelin in an age-dependent fashion especially in 3xTg mice. Taken together, extracellular SP-C, as modulator of glymphatic clearance and potential ligand of PNs, declines in 3xTg mice, which show an accumulation of extracellular Reelin depositions during ageing.

Introduction

Surfactant Protein C (SP-C) was initially described as lung-specific peptide, representing the smallest member of the heterogeneous Surfactant Protein (SP) family [1, 2] The latter comprises the immunologically active, lectin-type SPs (SP-A & SP-D) and the hydrophobic SPs (SP-B & SP-C), all of them being of paramount importance for the functionality of the pulmonary Surfactant [3]. This 'surface active agent', constituting only a small but substantial part of the alveolar fluid, most importantly decreases intra-alveolar surface tension [4] which contributes strongest to the elastic recoil of the lung, and therefore represents the primary counterforce of mechanical breathing [5]. Lack of surfactant, as it is often present in prematurely born infants, causes the respiratory distress syndrome (RDS), a condition that is characterized by alveolar collapse and associated with high mortality. The quantum satis of SPs within the Surfactant is imperative for normal respiratory function, as is demonstrated by the successful treatment of RDS with intra-pulmonary application of SP-containing Surfactant preparations [6].

The collectin-type SPs are closely linked to immunity, but SP-B and SP-C are also increasingly recognized as immunomodulatory peptides involved in host defence and dampening of inflammatory responses [2, 7-9]. Nevertheless, their most important function is to lower the alveolar surface tension.

Although there is substantial functional overlap between SP-B and SP-C [1], the latter has a number of distinctive and remarkable features; it is one of the most hydrophobic proteins [10], its sequence is the most conserved of all SPs [11] and its precursor, proSP-C, contains the BRICHOS domain, an intramolecular chaperone preventing amyloid formation, and thus, amyloid toxicity [12]. Recombinant BRICHOS from proSP-C has been demonstrated to efficiently delay formation of A β 40 and A β 42 fibrils [13]. *Vice versa*, mutant proSP-C has been linked causally to several progressive interstitial lung diseases exhibiting pulmonary amyloid deposition [14].

Both – SP-C and proSP-C – are not only present in the lungs [15]. In fact, the protein and its precursor are abundant at various physiological interfaces, for example the blood-testis-barrier [16], the blood-brain-barrier [15] and the blood-cerebrospinal-fluid-barrier [17]. More recent studies substantiate that SP-C, together with the other SPs, is involved in CSF rheology [18]. In detail, SP-C profiles in the CSF were not linked to CSF bulk flow, but significantly associated with white matter changes in context of impaired CSF clearance, indicating involvement of the paravascular clearance system [19, 20, 21]. Furthermore, a significant decline of CSF SP-C with increasing age has been demonstrated [20].

Considering the complex physiological profile of SP-C and its precursor proSP-C in the lungs, especially with respect to its function as chaperon and surface-active peptide, together with its expression in the CNS, comparable roles for CNS physiology are assumable.

The majority of neurodegenerative diseases, for example Parkinson's disease, Lewy Body dementia, and, most importantly Alzheimer's disease (AD), are related to protein misfolding and impaired paravascular clearance [22, 23], causing accumulation of detrimental metabolites, such as beta-amyloid, predominantly in the brain's extracellular matrix (ECM). Our study therefore aims to elucidate, whether SP-C / proSP-C are associated with the pathobiology of AD, for example the aggregation of non-functional Reelin deposits – a histological hallmark of disturbed Reelin signalling [24, 25]. For this purpose we applied a triple transgenic (3xTg) murine model with age-dependent Alzheimer-like neuropathological alterations [26]. Due to the yet limited knowledge on brain structures displaying SP-C-immunoreactivity (ir), a major goal of the present work was a more comprehensive qualitative analysis of SP-C-immunoreactive structures in the mouse forebrain. Additionally, focused on the pathobiology of AD, the study furthermore aimed for SP-C immunolabelling not only in combination with the detection of vascular, glial and neuronal components of the neurovascular unit (NVU), but also the evaluation of SP-C's spatial relationship to perineuronal nets (PNs). The latter represent a functionally significant specialised form of the ECM [27] and contribute to neuroprotection in AD, for example by inhibiting neuronal uptake of aggregated tau [28]. Furthermore, PNs are protective against oxidative stress and orchestrate synaptic plasticity, and hence, are of considerably increasing interest [29].

Materials And Methods

All animal experiments with a total of 122 mice of both genders were carried out according to the European Union Directive 2010/63/EU and were approved by the local authority (Regierungspräsidium

Leipzig; reference number T12/16). The animals had been bred in the Medizinisch-Experimentelles Zentrum of Leipzig University, starting with breeding pairs kindly provided by Drs Frank M. LaFerla and Dr. Salvatore Oddo (University of California, Irvine, CA, USA).

This work is largely based on triple transgenic (3xTg) mice which show age-dependent Alzheimer-like alterations in the brains such as tau hyperphosphorylation and β -amyloid deposits, as primarily described by Oddo et al [26] and manifold confirmed (see e.g. [30,31]). Wildtype (WT) 129/sv C57bl6 mice served for comparative analyses.

The histochemical part of the present study was performed with forebrain sections from 64 mice, whereas biochemical analyses were carried out with brain tissue from additional 58 animals comprised of WT and 3xTg mice as listed in Table 1.

Tissue preparation

For immunohistochemistry, mice were transcardially perfused with saline and 4 % phosphate-buffered paraformaldehyde. Next, the brains were post-fixed in the same fixative overnight and equilibrated in 30 % phosphate-buffered sucrose. Subsequently, forebrains were cut at 30 μ m thickness with a freezing microtome (Leica SM 2000R, Leica Biosystems, Wetzlar, Germany) resulting in 10 serial series each. All sections were collected in sealed vials filled with 0.1 M Tris-buffered saline, pH 7.4 (TBS) containing sodium azide and stored at 4°C.

For biochemical analyses, preparation of the brains after transcardial perfusion (as described above) was performed differently. As one aim of our study was to investigate the protein concentrations originating from different spaces, namely the intracellular compartment and the extracellular compartment, we applied a method initially introduced by Hofstein et al. in 1983 [32] and later on modified by Pulli et al. in 2013 [33].

Each mouse brain was halved; one hemisphere was used to obtain separated protein fractions originating from the extra- and intracellular compartment (according to [33]), the second hemisphere was used as separate sample omitting this step. All steps were performed on ice. In order to isolate the proteins from the extracellular compartment, the respective hemisphere was incubated with an extraction buffer consisting of 0.32 M sucrose (Roth, Karlsruhe, Germany), 1 mM CaCl_2 (Roth) and 10 U/ml heparin (ratiopharm GmbH, Ulm, Germany) in Hanks Balanced Salt Solution (HBSS) for 2h. Then, the hemisphere was removed from the buffer and kept on ice for further processing. Thereupon the protein containing extraction buffer was centrifuged at 1000 g for 5min. Subsequently, the supernatant was mixed with 4 parts of acetone and incubated overnight at 6°C to concentrate the diluted extracellular fraction. To precipitate the protein, the mixture was centrifuged at 3500 g for 15min at 4°C. Resulting supernatant was discarded and the pellet containing the protein was resuspended in PBS for subsequent protein quantifications. The hemisphere, which was kept on ice after extraction of the extracellular proteins, was subsequently homogenised with 1000 μ l of PBS. Fivehundred μ l of the homogenate were mixed with 500

µl of RIPA buffer (radioimmunoprecipitation assay buffer) and centrifuged at 15000 g for 20min. The supernatant containing the isolated proteins was used for further analysis.

The other, yet unprocessed hemisphere was also homogenised with 1000 µl of PBS. Fivehundred µl of the homogenate were mixed with 500 µl of RIPA and centrifuged at 15000 g for 20min to extract proteins without separating between the extracellular and intracellular compartment. The supernatant containing the isolated proteins of both, the extracellular and intracellular compartment, was stored for further analysis.

Immunofluorescence labelling

Prior to fluorescence labelling free-floating sections were extensively rinsed with TBS. Non-specific binding sites for subsequently applied immunoreagents were then blocked for 1 hour with 5 % normal donkey serum.

Immunolabelling of SP-C was performed with two antisera. The first was a rabbit antiserum recognising human proSP-C and its processing intermediates (raised against a recombinant fusion protein containing glutathione-S-transferase (GST) linked to the amino acids 1-20 from the N-terminal of the human proSP-C) and established for immunohistochemistry (see, e.g. [17]). This immunoreagent was obtained from Merck Millipore (Billerica, MA, USA) and generally used at 1:300 (in the blocking solution) for 20h. The second applied antiserum was a rabbit antiserum recognising the mature form of human surfactant protein C (human mature SP-C, established for immunoblots, see for example [34]). It was provided by Seven Hills Bioreagents (Cincinnati, OH, USA) and used at 1:400 (in the blocking solution) for 20h.

Sections were then rinsed with TBS and processed with carbocyanine (Cy2)-tagged donkey-anti-rabbit IgG [Dianova, Hamburg, Germany; 20 µg/ml TBS containing 2% bovine serum albumin (TBS-BSA)] for 1h. For triple fluorescence labelling, series of sections were incubated for 20h with rabbit-anti-SP-C combined with primary antibodies and biotinylated WFA or STL - diluted in the blocking solution - as listed in Table 2. Subsequently, the sections were washed with TBS and transferred for 1h into mixtures of appropriate fluorochromated, Cy-conjugated immunoreagents (all at 20 µg/ml TBS-BSA and obtained from Dianova, Hamburg, Germany) according to Table 1. Finally, sections were rinsed several times with TBS and briefly in distilled water, mounted onto fluorescence-free glass slides, air-dried and coverslipped with Entellan in toluene (Merck, Darmstadt, Germany).

Omission of primary antibodies or biotinylated lectins caused the expected absence of cellular labelling.

Microscopy, image processing and semi-quantification

For the screening of fluorescently labelled brain sections an Axioplan fluorescence microscope (Zeiss, Germany) was employed. For image acquisition a Bioevo BZ-9000 microscope (Keyence, Neu-Isenburg, Germany) was used, while highly magnified pictures were obtained with a confocal laser-scanning microscope LSM 880 from Zeiss. Microsoft PowerPoint (version 2015; Microsoft Corp., Redmond, WA,

USA) was applied to create panels of micrographs. In a few cases, brightness and contrast of micrographs were slightly adjusted without deleting or creating signals.

The semi-quantification of hippocampal dots based on 4 to 6 immunolabelled sections from all mice. All sections were digitised by means of a digital slide scanner (Pannoramic Scan II, 3D HISTECH Ltd., Budapest, Hungary) equipped with a quad band (DAPI/FITC/TRITC/Cy5) filter set. The FITC filter was used for the detection of Cy2 and the TRITC filter for the visualization of Cy3. Next, the hippocampal region in both hemispheres was delineated and exported from slide scanner data sets (Case Viewer, Version 2.3.0.99276, 3D HISTECH Ltd.) as raster images with pixel dimensions of 0.325 μm .

Image analysis was performed with Mathematica (Version 12.0, Wolfram Research, Inc., Champaign, IL, USA). Images were imported and split into separate colour channels. Red image channel was inverted and subtracted from green image channel, followed by Kittler-Illingworth minimum error thresholding [35]. Segmentation results were subsequently exported and cleared of falsifying artefacts such as intraluminal precipitates or overlapping tissue overlays manually (GNU Image Manipulation Program, version 2.8, The GIMP team, <http://www.gimp.org>). Corrected segmentation images were imported into Mathematica, areas of total tissue as well as segmented dots were computed, and ratio of dot to tissue area was calculated.

Biochemical analysis

After obtaining the three distinct protein isolates from each mouse brain – extracellular, intracellular and non-separated whole hemisphere (from here on referred to as 'total'), the samples were further analysed in order to estimate the total protein content using a Pierce Bicinchoninic Acid (BCA) protein assay (Thermo Fisher Scientific) and the levels of SP-C and Reelin (ELISA kits for murine SP-C and Reelin; Cloud-Clone Corp., Fernhurst, TX, USA).

Quantification of total protein, SP-C and Reelin was performed according to the manufacturers' instructions using a microplate spectrophotometer at a wavelength of 450 nm.

Finally, the concentration of the proteins of interest, SP-C and Reelin, was normalised to the total protein content of each sample.

Statistical Analysis

Statistical analysis was performed using IBM SPSS Statistics (Version 25, IBM Corp., Armonk, New York, USA). In a first step, descriptive statistics comparing age-matched triple transgenic and wildtype animals (3, 6, 12, 18 and 24 months) were calculated. Box plots were generated in order to visually facilitate the group comparisons. Furthermore, WT and 3xTg animals were analysed separately in order to detect age-dependent changes in the respective animal group. Data was tested for normal (Gaussian) distribution using the Shapiro-Wilk-Test. Depending on the results of the latter, comparisons between age-matched

WT and 3xTg animals (two groups per test), comparisons between differently aged groups of wildtype animals and of 3xTg mice (four groups per test each) were performed using either Students T-Test (Gaussian distribution, two groups), Mann-Whitney-U-Test (non-Gaussian distribution, two groups) or Kruskal-Wallis-Test and Jonckheere-Terpstra-Test (non-Gaussian distribution, more than two groups). Significance was set at $p < 0.05$. In a last step, Spearman-Rho (non-Gaussian distribution) and Pearson's Coefficient (Gaussian distribution) were calculated in order to identify significant correlations between the investigated biomarkers, i.e. SP-C and Reelin.

Results

Fluorescence labelling

The detection of SP-C in serial sections comprising the forebrain of young adult and aged mice led to novel findings such as the strong cellular labelling in the medial habenula (Fig. 1a) and confirmed previously obtained data [17]. Confocal laser-scanning of hippocampal tissue at higher magnification for the first time revealed SP-C-immunoreactive structures, as exemplified in Fig. 1b by a ramified, glia-shaped cell, in vicinity to clustered dots. The latter resemble structures which were previously reported by Knuesel et al for Reelin [36], Butkevich et al. for the protein FEZ1 [37] and by Jucker, Walker and co-workers for a laminin-binding protein [38, 39]. Notably, the infundibulum exhibited strong SP-C immunolabelling of fibrous structures but was devoid of concomitantly visualised AQP-4-ir (Fig. 1d), which remained restricted to the adjoining brain parenchyma. This region also displays strongly stained vessels by applying biotinylated STL (Fig. 1e). Additionally, this lectin heavily marked the ependymal rim of the infundibulum. The overlay of staining patterns in Fig. 1f primarily clarified the complementary distribution of immunosignals for SP-C and AQP-4.

Further triple fluorescence labelling demonstrated the absence of SP-C-ir in GFAP-expressing astroglia, in processes immunopositive for the oligodendroglial marker RIP and in microglia stained with antibodies directed the ionized calcium binding adapter molecule-1 (Iba; Fig. 2a-d). Notably, SP-C-ir was found in a subset of S100 β -containing astrocytes in the corpus callosum (arrows in Fig. 2e). Moreover, a high power confocal image of this region demonstrated an SP-C-immunoreactive rim of such S100 β -immunopositive cells apart from GFAP-containing fibres (Fig. 2f).

Next, combined detection of SP-C, S100 β and a further oligodendroglial marker, 2',3' cyclic nucleotide phosphodiesterase (CNP), as shown in Fig. 3, clearly elucidated that CNP-positive structures were devoid of SP-C immunostaining, while S100 β -containing astroglia - co-labelled with SP-C (arrows in Fig. 3d) - were visualised by strong red fluorescent Cy3 (instead of Cy5 as illustrated in Fig. 2e,f). Additional robust SP-C-ir was observed in the indusium griseum (asterisk) and in the granular layer of the hippocampal CA1 region (arrows). In Fig. 3e-h, the combined immunodetection of SP-C, S100 β and neuronal nuclei (NeuN) revealed the frequent association of all three markers as exemplified for the nucleus reticularis thalami (NRT) and the ventral pallidum. Thereby, the NRT displayed the strongest SP-C immunostaining (Fig. 3e,h).

The counterstaining of SP-C-ir by parvalbumin (PARV) as a marker for GABAergic interneurons detected partly overlapping neocortical distribution patterns as shown for the retrosplenial cortex of 3-month-old WT mice (Fig. 4a,b). Additional lectin-histochemical staining with biotinylated WFA and Cy3-streptavidin revealed numerous PNs (Fig. 4c). Their well-known ensheathment of many PARV-containing neurons became clearly visible, as well as many SP-C and PARV co-expressing neurons (Fig. 4d). In Fig 4e, Z stacks of confocal images at higher magnification elucidated faint SP-C-ir within the rim and proximal dendrites of several neurons and somewhat stronger stained ramified cells with smaller cell bodies together with the counterstaining of the net markers WFA and ACAN in the same area. The overlay also demonstrated the close vicinity of SP-C-stained neuronal rims and surrounding net components.

Indicating their heterogeneity, PNs appeared either double-stained by WFA and ACAN or mono-labelled by only one marker. These findings were strongly supported by Fig. 4f, showing a representative confocal image from the retrosplenial cortex, which was triple-stained for SP-C, WFA and HAPLN1 (hyaluronan and proteoglycan link protein 1 = link protein = CRTL1).

Further triple fluorescence labelling of the NRT detected that SP-C was allocated with lectin- and immunohistochemically stained PNs in the NRT but remained without counterstaining in the adjacent ventral pallidum (Fig. 5a,d) and globus pallidus (Fig. 5e,h). Notably the staining of WFA-binding sites (Fig. 5b) appeared somewhat stronger than the immunolabelling with mouse-anti ACAN (Fig. 5c). Fig. 5d displays WFA/ACAN-double-stained nets as mixed colour purple and their co-occurrence with SP-C in white. The heavy and – in this brain region exclusively occurring – red fluorescent WFA-staining (Fig. 5f) appeared as a carpet for numerous enwrapped PARV-ir, also outlining the NRT. The association of all three markers (SP-C, WFA, PARV) was again visible by many white-appearing structures in the NRT.

The lateral hypothalamic area (LHA) was a further, newly identified region showing numerous structures with SP-C-ir, perineuronal net markers and S100 β in close proximity (Fig. 6a-h). Yellowish staining indicated in Fig. 6d co-occurring SP-C and S100 β , whereas and white staining revealed the close vicinity of both markers and WFA-binding sites. Many SP-C-ir neurons were enwrapped by PNs stained either with WFA (Fig. 6b,f) or anti-neurocan (NCAN, Fig.6g). The lectin-histochemical staining appeared clearer contoured and usually stronger than the immunolabelling that dominated only in parts of the neuropil (Fig. 6h).

Analysing hippocampal sections triple-stained for SP-C, WFA and either ACAN (Fig. 7a-d) or NCAN (Fig. 7e-h), the close vicinity of SP-C (Fig. 7a,e) and lectin-binding sites (Fig. 7b,f) was pronounced in the CA2 area, known to be selectively detectable by the visualisation of PNs. While ACAN is partly present in clearly contoured PNs (Fig. 7c), the adjacent tissue displayed a diffuse NCAN immunolabelling (Fig. 7g). The overlay clearly indicated WFA/ACAN double-positive PNs (appearing purple) allocated with SP-C-ir. Notably, SP-C-ir was also observed in granular cells and their dendrites in the CA1 region (Fig. 7a,e). In the gyrus dentatus, the simultaneous detection of SP-C (Fig 7i), WFA (Fig. 7j) and VGAT (Fig. 7k) revealed their co-occurrence as clarified by merging their distribution patterns (Fig. 7l). On the contrary, clusters of dots in the stratum lacunosum-moleculare remained mono-labelled for SP-C.

For the combined detection of SP-C-ir dots, PNs and glutamatergic axonal endings, triple fluorescence labelling included the detection of vesicular glutamate transporters (VGLUT) 1 and VGLUT2, respectively (Fig. 8a-h). While the gyrus dentatus showed expected cellular SP-C-ir cell layers and two clusters of dots in the fissura hippocampalis (Fig. 8a), the subiculum displayed faintly labelled SP-C-immunopositive cells and plaque-like deposits (Fig. 8e). In parallel, WFA labelling was strong in the gyrus dentatus (Fig. 8b), but only loosely distributed in the subiculum (Fig. 8f). Red fluorescent counterstaining of VGLUT-ir dominated in the hilus (Fig. 8c,d), whereas the subiculum exhibited deposits composed of dots (with apparently larger diameters than those containing SP-C), oftentimes forming rosette-like clusters (Fig. 8g). Such structures occasionally appeared plaque-associated in the overlay of staining patterns (Fig. 8h), which also indicate the allocation of SP-C-ir and WFA-binding sites by turquoise colour.

As a next step, the spatial relationships of SP-C- and VGLUT2-ir deposits with the age-dependent formation and hyperphosphorylated protein tau (Fig. 9a-d) and A β plaques (Fig. 9e-h) were exemplarily revealed in the subiculum from 22-month-old 3xTg mice. Thereby, the different location of green fluorescent SP-C dots (Fig. 9a,d,e,h) and red fluorescent VGLUT2-ir deposits (Fig. 9b,d,f,h) was primarily confirmed. Moreover, SP-C- and VGLUT2-ir were neither co-localised with A β plaques (detected with biotinylated mouse-anti-A β ₁₈₋₂₃, Fig. 9h) nor with microtubule-associated protein tau (detected with biotinylated AT8 recognising phospho-serine₂₀₂ and phospho-threonine₂₀₅, Fig. 9d). The merged staining patterns clarified that all age-dependent deposits occurred separately in the subiculum and adjacent tissue from 22-month-old 3xTg mice.

Searching for further markers of SP-C-immunopositive dots, hippocampal sections were applied to Cy3-staining of Reelin (red) as exemplarily shown at lower magnification for 3-month-old- (Fig. 10a) and 16-month-old WT mice (Fig. 10b). Additionally, the same sections were counterstained with goat-anti-aquaporin 4 (AQP4; colour-coded in blue) in order to clarify the spatial relationships between vessel-associated astroglial endfeet and clusters of dots. At higher magnification, the younger animals exhibited several, partly clustered dots in the fissura hippocampalis, immunopositive both for SP-C (Fig. 10c) and Reelin (Fig. 10d) as clarified by the overlay (Fig. 10f). In the same area, the vascular AQP4 staining (Fig. 10e,f) appeared even stronger than in other parts of the hippocampal formation. Compared with young mice, the aged WT mice displayed more solitary dots and clusters containing SP-C (Fig. 10g) and Reelin (Fig. 10h), as demonstrated here for the stratum radiatum and the stratum lacunosum-moleculare in the CA1 region. A strong AQP4 staining demarcated not only the vessels (Fig. 10i) but was also the surrounding neuropil (Fig. 10j). Additionally, several vessels appearing pink were found to be double-labelled by concomitant staining for Reelin and AQP4, but devoid of SP-C-ir.

In the medial habenula, additional immunofluorescence labelling of mature SP-C revealed a staining pattern of less clearly marked cells that slightly differed from proSP-C immunolabelling (Fig. 11a). On the contrary, hippocampal dots immunopositive for mature SP-C in 16-month-old 3xTg mouse (Fig. 11b) and an age-matched WT mouse (Fig. 11c) largely resembled the clusters visualised by anti-proSP-C. Counterstaining of WT tissue with Reelin (Fig. 11d) also revealed numerous clusters of dots. The overlay (Fig. 11e) elucidated predominantly double-stained yellowish structures, but also a few slightly reddish

dots mono-labelled for Reelin. Expectedly, a large proportion of the clusters was located near the fissura hippocampalis with its strong vascular staining for AQP4 (Fig 11 e). Notably, the granule layer of the presented case remained devoid of immunosignals for mature SP-C.

For the semiquantitative estimation of age-dependent changes of dots and their clusters in the hippocampi from WT and 3xTg mice, the relation between the area of SP-C-stained dots and the corresponding whole hippocampal area was comparatively determined using serial sections after triple-staining for SP-C, Reelin and AQP4.

Overall, 32 WT mice were investigated. The proportion of dots in the 3-month-old WT group was significantly lower ($p < 0.05$) than in all other age groups of the cohort (6, 12, 16 and approximately 24 months). Comparable data were also obtained for 6-month-old mice and their respective older counterparts. However, there was no significant difference between the mice of 12, 16 and approximately 24 months.

A total of 32 3x-Tg mice belonging to 5 differently aged groups were examined. The 3-month-old ones as well as the 6- and 12-month-old mice had a significantly ($p < 0.05$) lower proportion of dots per hippocampus than the respective older age groups. There was no significant difference between 6-month-old and 12-month-old mice. Similarly, there was no significant difference between the dot area of 16 month-old 3x-Tg mice and their older counterparts.

A comparison of the surface area of the deposits on the hippocampal surface revealed that there was no significant difference between the WT and the 3x-Tg mice aged 6, 12 and 16-months. However, in the 3-month-old group and in the more than 22-month-old mice, the area fraction of dots was significantly ($p < 0.05$) higher in 3xTg mice than in the respective WT groups.

Immunoassays – SP-C and Reelin in wildtype and triple transgenic mice

Table 3 summarises the descriptive statistical analysis of all WT and 3x-Tg mice, allowing a direct comparison of the concentrations of the proteins of interest between both groups in an age-matched manner. The results of significance testing for the comparative analysis of both groups are provided below. Subsequently, WT and 3x-Tg mice are analysed separately.

In the group of 3-month-old animals Gaussian distribution was identified for all fractions of SP-C and Reelin. In brief, extracellular Reelin ($p = 0.05$), intracellular Reelin ($p < 0.01$) and total Reelin ($p < 0.01$) were significantly higher in 3x-Tg mice compared to WT mice. All fractions displayed no significant differences in SP-C levels between both groups. Boxplots in Figs 12a,b graphically summarise the findings.

In the group of 6-month-old animals, the only non-normally distributed fraction was total Reelin. On the contrary, intracellular and extracellular Reelin as well as all fractions of SP-C were distributed normally. Differences between both groups achieving statistical significance were identified as follows.

Extracellular SP-C ($p=0.013$), intracellular SP-C ($p=0.008$) and total SP-C ($p=0.001$) were significantly higher in the WT group. Extracellular Reelin ($p=0.001$), intracellular Reelin ($p=0.001$) and total Reelin ($p=0.001$) were significantly higher in the 3x-Tg group. The boxplots in figure 12 c and d graphically summarise the differences between both groups.

In the group of 12-month-old animals, all SP-C fractions were distributed normally, whereas the different Reelin fractions exhibited non-Gaussian distribution.

Differences between groups achieving statistical significance were revealed in the following manner: Extracellular SP-C ($p=0.023$) and intracellular SP-C ($p=0.030$) were higher in the WT group. Extracellular Reelin ($p=0.006$), intracellular Reelin ($p=0.004$) and total Reelin ($p=0.004$) were significantly higher in the 3x-Tg group. Boxplots in figure 12 e and f graphically summarize the differences between both groups.

For the analysis of very old mice, only 3x-Tg animals of 16 months, not older ones, were available for protein quantification. However, WT animals of 16 months and older (24 months) were available. All tests were performed in an exactly age-matched manner and additionally compared 16-month-old 3x-Tg mice with 16-24-month-old WT mice. Due to the lack of significant differences between both comparisons we report only the more comprehensive, latter comparison.

In the group of very old mice, Gaussian distribution was identified only for SP-C from the extracellular compartment. All other protein fractions were distributed non-normally.

Contrary to the younger animals, there were no significant differences regarding extracellular or intracellular SP-C levels or total SP-C levels. However, a trend of higher extracellular SP-C in the WT animals was observable ($p=0.176$) compared to 3xTg animals. Regarding Reelin, however, the differences were similar compared to the younger animal groups. Reelin concentrations of all origins were significantly higher in 3x-Tg animals (extracellular Reelin: $p<0.001$, intracellular Reelin: $p<0.001$ and total Reelin: $p=0.002$) compared to WT mice. Boxplots in Fig, 12g,h graphically summarise the differences between both groups.

SP-C and Reelin in 3x-Tg mice – age dependency and correlations

Gaussian distribution was recognised for extracellular and total SP-C and for extracellular- as well as total Reelin. Significant differences between 3x-Tg animals of different ages were identified for intracellular Reelin ($p=0.019$) and total Reelin ($p=0.022$). A remarkable trend of decreasing extracellular SP-C with growing age was observed, but did not reach statistical significance ($p=0.076$, Fig 13 a,c). Intracellular Reelin decreased from 3-month-old to 6-month-old mice and then revealed a steady increase from 6- to 16-month-old mice. Total Reelin increased from 3- to 16-month-old mice in a linear fashion.

Extracellular SP-C decreased with increasing age, showing stagnation in 6- and 12-month-old mice, and then a further decrease after the age of 12 months. In comparison, the extracellular SP-C fraction constituted slightly more than half of the total SP-C concentration.

The grouped boxplots in Fig. 13a,b provide an overview over the differences in Reelin- and SP-C concentrations from the different fractions at the different ages in 3x-Tg mice. The simple boxplots in Fig. 13c,d,f demonstrate relevant differences as described above.

With regard to the relationship between the investigated proteins, the following correlations were identified: Extracellular SP-C showed an inverse correlation with extracellular Reelin ($r=-0.780$, $p<0.001$). In line with the group comparison testing, the inverse relationship between extracellular SP-C and age did not achieve statistical significance ($r=-0.307$, $p=0.099$). Total SP-C correlated with total Reelin ($r=0.540$, $p=0.002$). Interestingly, total SP-C showed a (in contrast to extracellular SP-C non-inverse) trend of correlation with age ($r=0.314$, $p=0.098$). Total Reelin correlated with age ($r=0.420$, $p=0.023$).

The scatterplots in Fig. 13e,g show the most relevant identified correlations between SP-C and Reelin fractions.

SP-C and Reelin in WT mice – age dependency

Gaussian distribution was recognised for intracellular Reelin. The remaining protein fractions exhibited non-Gaussian distribution. Significant differences between 3x-Tg animals of different age were identified for total SP-C ($p=0.037$) and intracellular Reelin ($p=0.020$). A trend without statistical significance was observable for total Reelin ($p=0.069$).

Intracellular Reelin showed a clear decrease with increasing age of WT mice. Total Reelin was high in 3- and 6-month-old animals and then decreased to a comparatively similar, lower level in older animals.

Extracellular SP-C showed an increase from 3- to 12-month-old mice, followed by a decrease in 16-month-old mice and a significant increase with the age of 24 months, but without achieving statistical significance ($p=0.186$). Total SP-C was low in 3-month-old mice, increased significantly in 6-month-old mice and dropped again to a steadily low level in 12-24-month-old animals ($p=0.037$).

The grouped boxplots in Fig. 14a,b provide an overview over the differences in Reelin- and SP-C concentrations from the different fractions at the different ages in WT mice. The simple boxplots in Fig. 13c,d demonstrate relevant differences as described above.

Regarding the relationship between the investigated proteins, the following correlations were identified. Extracellular SP-C showed a strong, inverse correlation with extracellular Reelin ($r=-0.694$, $p<0.001$). Intracellular SP-C correlated significantly with intracellular Reelin ($r=0.510$, $p=0.007$). Total SP-C correlated with total Reelin ($r=0.598$, $p=0.002$). Interestingly, total SP-C showed a non-significant (contrary to triple transgenic mice inverse) trend of correlation with age ($r=-0.325$, $p=0.098$). Intracellular Reelin correlated inversely with age ($r=-0.444$, $p=0.020$).

The scatterplots in Fig. 14e,f ,g show the most relevant identified correlations between SP-C and Reelin fractions. The scatterplots in Fig. 14h,i show the identified significant correlations between SP-C / Reelin fractions and age.

Synopsis of biochemical findings

In general, higher Reelin levels (all fractions) were associated with 3x-Tg mice in the age-matched comparison. Contrary to this finding, extracellular SP-C was significantly lower in 6- and 12-month-old 3x-Tg mice than in respective WT mice. Extracellular SP-C remained lower in 3x-Tg mice older than 12 months, but the difference did not remain statistically significant.

Significant inverse correlations were found between extracellular SP-C and extracellular Reelin in all ageing groups.

When considering 3x-Tg mice only, Reelin (all fractions) increased with growing age, whereas extracellular SP-C decreased with age.

When considering WT mice only, Reelin (intracellular and total) decreased with growing age, whereas extracellular SP-C showed a trend of increase with growing age.

Discussion

To our best knowledge, this study is the first investigating age-dependent distribution, morphology and concentrations of pro-SP-C / SP-C in brains of WT and 3x-Tg mice, with special attention given to the association of SP-C with PNs and Reelin.

Putting the primary focus on the distribution of SP-C in the different brain compartments, it is already remarkable to note that extracellular SP-C accounted for slightly more than half of the absolute amount of cerebral SP-C. Considering its well-established importance for the physicochemical properties of the alveolar fluid layer, this novel finding substantiates the hypothesis of SP-C's contribution to interstitial- and cerebrospinal fluid rheology, and therefore, its involvement in brain waste clearance [20, 21].

Additionally, the distinct alterations of extracellular SP-C in WT mice, showing an increase with age, versus the diametrical, age-dependent decrease of extracellular SP-C in 3xTg mice, who suffer from AD-like neuropathological changes, further indicate an intrinsically neuro-protective function of cerebral SP-C.

However, one primary hypothesis of our study was the potential role of pro-SP-C's anti-amyloid chaperone activity for preventing AD-related neuropathological changes, as pro-SP-C harbours the BRICHOS domain, which has been shown to counteract amyloid fibril formation [40]. Surprisingly, combined immunofluorescence labelling of BRICHOS and pro-SP-C did not reveal co-labelled structures such as dots. On the contrary, a well-established antibody, designed to exclusively detect the mature form of SP-C [34] produced staining patterns, which largely resembled those obtained with antibodies directed against proSP-C. These results lead to the conclusion that the form of cerebral SP-C, which we detected, is not the BRICHOS-containing SP-C precursor (21kDa) [41], but late intermediates (12-16kDa) and the mature SP-C (4kDa), which is in line with the first report on the cerebral Surfactant Protein System, that found late

intermediates and the mature form of SP-C in brain tissue and cerebrospinal fluid [17]. Thus, pro-SP-C appears to play no significant role as CNS-intrinsic chaperone preventing A β formation.

Reelin, an extracellular glycoprotein involved in memory and learning by modulating synaptic plasticity has been shown to limit tau hyperphosphorylation and amyloidogenic processing of the β -amyloid precursor protein comparatively upstream in the respective AD-relevant pathway [42, 43]. *Vice versa*, age-related aggregation - and thus concomitant reduction of functional Reelin - are linked to synaptic dysfunction together with enhanced formation of β -amyloid and tau hyperphosphorylation [25]. Considering Reelin's role as a proximal molecular player in the orchestra of AD pathways, its age-dependent propensity to form deposits, which are pronounced in a murine AD model [25] and its abundance in the extracellular space, Reelin was implemented in our study as protein of reference for interpretation of SP-C changes in context of AD.

In general, our study for the first time revealed a significant inverse correlation between extracellular Reelin and extracellular SP-C and confirmed statistically significant age-dependent changes of SP-C in both animal groups. The contrasting trends of SP-C- and Reelin-concentrations in the extracellular compartment comprehensibly represent pathophysiologically synergistic alterations in context of AD, as an increase of Reelin deposits is linked to loss of synaptic function and a decrease of SP-C is associated with disturbed glymphatic clearance and progressive white matter disease [21].

Therefore, amalgamating current and novel insights on Reelin and SP-C with respect to AD pathobiology – decreased levels of extracellular SP-C, accompanying reduced glymphatic clearance - are associated with increased deposition of non-functional Reelin in the extracellular compartment of 3xTg mice.

Furthermore, the present study provides novel data on chemical neuroanatomy, such as a first description of astrocytes in the corpus callosum, which co-express SP-C and the dimeric calcium-binding protein S100 β (Fig. 2h, 3d). Notably, S100 β is widely considered as astroglial marker and strongly elevated in activated astrocytes surrounding neuritic plaques [44], the latter representing a potential molecular indicator for brain damage [45]. Moreover, S100 β was revealed as damage-associated molecular pattern (DAMP) molecule triggering tissue reactions to damage in a series of different neural disorders [46]. Although Steiner et al. showed a wide extra-astrocytic distribution of S100 β and suggested to carefully discuss the astroglial nature of S100 β -immunopositive cells [47], our study revealed cells co-expressing SP-C and S100 β without exhibiting immunoreactivity for the oligodendroglial markers RIP (Fig. 2d) and CNP (Fig. 3d) or microglial Iba-ir (Fig. 2h), confirming their astroglial lineage. The regulation of S100 β in 3x-Tg mice is beyond the scope of this study, however, our results support earlier reports that demonstrated a contribution of S100 β - (and SP-C-) producing astrocytes to the pathobiology of AD [48].

Unexpectedly, SP-C-ir was found to be allocated with PNs. These polyanionic, chondroitin sulphate proteoglycan (CSPG)-rich, lattice-like coatings surround certain neurons in several parts of mammalian brains [27]. They were already observed by Ramón y Cajal, and based on sophisticated histological stainings, described by Camillo Golgi [49]. Brauer and co-workers coined the term “perineuronal nets” [50]. Currently, a widely applied method for the visualisation of a large portion of PNs is the lectin-

histochemical staining with the N-acetylgalactosamine-recognising *Wisteria floribunda* agglutinin (WFA) [51]. A portion of PNs is not detectable by WFA, but immunopositive for their main CSPG component aggrecan, as reported for instance for the murine hippocampus [52], whereas WFA-stainable, aggrecan-immunonegative PNs were found in the mouse entorhinal cortex [53] and are also demonstrated in the present study (see Fig. 4d). While in the neocortex and numerous further brain regions WFA-binding sites surround predominantly fast-firing, parvalbumin-containing GABAergic neurons [54, 55], a considerable portion of nets enwraps neurons containing other neurotransmitters [56]. Notably, net-bearing cholinergic neurons were detected in the human nucleus abducens [57] and in the rat spinal cord [58].

PNs might serve as rapid cation exchangers around fast-firing and 'active' neurons [54] and act as diffusion barriers with ion sorting properties [59]. Additionally, they suppress synaptic plasticity around net-bearing neurons [60, 61], a fact that was clearly demonstrated for CA2 pyramidal neurons [62, 63], which express excitatory calcium-calmodulin-dependent protein kinase II (CamKII) [64]. Moreover, PNs were attributed to the consolidation of memories [65 - 67] and in the prefrontal cortex they may contribute to cognitive function [68].

Neuropathological alterations of PNs and associated cells were reported for several diseases such as epilepsy [69, 70], addiction [71], schizophrenia [72] and amyotrophic lateral sclerosis [73]. After ischemic stroke, PNs are drastically damaged or even erased [74, 75]. In AD, net-bearing neurons are hardly affected by tau pathology indicating neuroprotective properties of certain net components [76, 77]. Noteworthy, PNs also protect against oxidative stress [78, 79]. Recently, several reviews summarised the previously mostly underestimated role of PNs in health and disease [80 - 83].

Functionality of PNs is also related to non-covalently bound ligands, for example the chemorepulsive protein semaphorin 3A [84, 85]. Notably, neuronal pentraxin 2 (Nptx2), an important regulator of α -amino-3-hydroxy-5-methyl-4-isoxazolepropionic acid (AMPA) receptors, binds PNs and enhances their formation [86]. Moreover, Otx2 – a net-associated modulator of neuronal plasticity even during adulthood [87] – prototypically binds to the polyanionic sites of PNs via an arginine-lysine motif and thereby restores neuronal plasticity for example in the visual cortex [88].

Similarly, the arginyl-lysyl sequence of extracellularly released SP-C might interact with the negatively charged PNs, whereas the intracellular SP-C fraction displays these N-terminal juxtamembrane positively residues in the cytosol [41, 89]. The co-localization of SP-C and PNs shown here for the first time, together with the neuronal SP-C expression pattern, indicate a functional role of SP-C in association with PNs. However, lying beyond the scope of this study, future investigations are needed to further elucidate the functional role of SP-C as ligand for PNs, for example at electron microscopic level.

Declarations

Acknowledgements

The authors thank Stephan Altmann for excellent technical assistance.

Funding

We acknowledge support from the Medical Faculty of the University Leipzig *via* the Clinician Scientist Program.

Competing interests

The authors declare no competing interests.

Availability of Data and Materials

All relevant data is included in the manuscript.

Author contributions:

JP performed experiments, analysed the data, and wrote the manuscript. KW performed image analysis and quantification. DM provided assistance during figure preparation and reviewed the manuscript. BM prepared tissues to be analysed and reviewed the manuscript. HM supported experiments and reviewed the manuscript. AE analysed the data and reviewed the manuscript. FG reviewed the paper. K-TH wrote and reviewed the paper. AM performed experiments and imaging, MK analysed the data and performed experiments. WH and SS designed the study, performed experiments and wrote the manuscript. All authors read and approved the manuscript

Ethics approval and consent to participate

All animal experiments were performed according to the European Union Directive 2010/63/EU and were approved by the local authority (Regierungspräsidium Leipzig; reference number T12/16). The study did not involve human samples, therefore consent to participate does not apply.

Consent for publication: not applicable.

References

1. Ketko AK, Donn SM (2009) Surfactant-associated proteins: structure, function and clinical implications. *Curr Pediatr Rev* 10:162-167. <https://doi.org/10.2174/157339631130900006>
2. Sunde M, Pham CLL, Kwan AH. Molecular Characteristics and Biological Functions of Surface-Active and Surfactant Proteins (2017) *Annu Rev Biochem* 86:585-608. <https://doi.org/10.1146/annurev-biochem-061516-044847>
3. Beers MF, Wali A, Eckenhoff MF, Feinstein SI, Fisher JH, Fisher AB (1992) An antibody with specificity for surfactant protein C precursors: identification of pro-SP-C in rat lung. *Am J Respir Cell Mol Biol* 7:368–378. <https://doi.org/10.1165/ajrcmb/7.4.368>

4. Jeon GW (2019) Surfactant preparations for preterm infants with respiratory distress syndrome: past, present, and future. *Korean J Pediatr* 62:155–161. <https://doi.org/10.3345/kjp.2018.07185>
5. Halliday HL (2008) Surfactants: past, present and future. *J Perinatol* 28 (Suppl1):S47 -56. <https://doi.org/10.1038/jp.2008.50>
6. Enhörning G, Robertson B (1972) Lung expansion in the premature rabbit fetus after tracheal deposition of surfactant. *Pediatrics* 50:58–66
7. Jin H, Ciechanowicz AK, Kaplan AR, Wang L, Zhang P-X, Lu Y-C et al (2018) Surfactant protein C dampens inflammation by decreasing JAK/STAT activation during lung repair. *Am J Physiol Lung Cell Mol Physiol* 314:L882-L892. <https://doi.org/10.1152/ajplung.00418.2017>
8. Tafel O, Latzin P, Paul K, Winter T, Woischnik M, Griese M (2008) Surfactant proteins SP-B and SP-C and their precursors in bronchoalveolar lavages from children with acute and chronic inflammatory airway disease. *BMC Pulm Med* 8:6. <https://doi.org/10.1186/1471-2466-8-6>
9. Venosa A, Katzen J, Tomer Y, Kopp M, Jamil S, Russo SJ et al (2019) Epithelial Expression of an Interstitial Lung Disease-Associated Mutation in Surfactant Protein-C Modulates Recruitment and Activation of Key Myeloid Cell Populations in Mice. *J Immunol* 202:2760-2771. <https://doi.org/10.4049/jimmunol.1900039>
10. Brown NJ, Johansson J, Barron AE (2008) Biomimicry of surfactant protein C. *Acc Chem Res* 41:1409-1417. <https://doi.org/10.1021/ar800058t>
11. Haagsman HP, Diemel RV (2001) Surfactant-associated proteins: functions and structural variation. *Comp Biochem Physiol A Mol Integr Physiol* 129:91–108. [https://doi.org/10.1016/S1095-6433\(01\)00308-7](https://doi.org/10.1016/S1095-6433(01)00308-7)
12. Knight SD, Presto J, Linse S, Johansson J (2013) The BRICHOS domain, amyloid fibril formation, and their relationship. *Biochemistry* 52:7523-7531. <https://doi.org/10.1021/bi400908x>
13. Cohen SIA, Arosio P, Presto J, Kurudenkandy FR, Biverstal H, Dolfe L et al (2015) A molecular chaperone breaks the catalytic cycle that generates toxic A β oligomers. *Nat Struct Mol Biol* 22:207-213. <https://doi.org/10.1038/nsmb.2971>
14. Peca D, Boldrini R, Johansson J, Shieh JT, Citti A, Petrini S et al (2015) Clinical and ultrastructural spectrum of diffuse lung disease associated with surfactant protein C mutations. *Eur J Hum Genet* 23:1033-1041. <https://doi.org/10.1038/ejhg.2015.45>.
15. Schob S, Dieckow J, Fehrenbach M, Peukert N, Weiss A, Kluth D et al (2017) Occurrence and colocalization of surfactant proteins A, B, C and D in the developing and adult rat brain. *Ann Anat* 210:121-127. <https://doi.org/10.1016/j.aanat.2016.10.006>

16. Beileke S, Claassen H, Wagner W, Matthies C, Ruf C, Hartmann A et al (2015) Expression and Localization of Lung Surfactant Proteins in Human Testis. PLoS One 10:e0143058. <https://doi.org/10.1371/journal.pone.0143058>
17. Schob S, Schicht M, Sel S, Stiller D, Kekulé AS, Paulsen F et al. (2013) The detection of surfactant proteins A, B, C and D in the human brain and their regulation in cerebral infarction, autoimmune conditions and infections of the CNS. PLoS One 2013;8:e74412. <https://doi.org/10.1371/journal.pone.0074412>
18. Krause M, Peukert N, Härtig W, Emmer A, Mahr CV, Richter C et al. Localization, Occurrence, and CSF Changes of SP-G, a New Surface Active Protein with Assumable Immunoregulatory Functions in the CNS. Mol Neurobiol. 2019; 56:2433-2439. <https://doi.org/10.1007/s12035-018-1247-x>
19. Bakker EN, Bacskai BJ, Arbel-Ornath M, Aldea R, Bedussi B, Morris AW et al (2016) Lymphatic Clearance of the Brain: Perivascular, Paravascular and Significance for Neurodegenerative Diseases. Cell Mol Neurobiol 36:181-194. <https://doi.org/10.1007/s10571-015-0273-8>
20. Schob S, Weiß A, Surov A, Dieckow J, Richter C, Pirlich M et al (2018) [Elevated Surfactant Protein Levels and Increased Flow of Cerebrospinal Fluid in Cranial Magnetic Resonance Imaging](#). Mol Neurobiol 55:6227-6236. <https://doi.org/10.1007/s12035-017-0835-5>
21. [Weiß A, Krause M, Stockert A, Richter C, Puchta J, Bhogal P et al \(2019\) Rheologically Essential Surfactant Proteins of the CSF Interacting with Periventricular White Matter Changes in Hydrocephalus Patients - Implications for CSF Dynamics and the Glymphatic System](#). Mol Neurobiol 56:7863-7871. <https://doi.org/10.1007/s12035-019-01648-z>
22. Araki K, Yagi N, Aoyama K, Choong C-J, Hayakawa H, Fujimura H et al (2019) Parkinson's disease is a type of amyloidosis featuring accumulation of amyloid fibrils of α -synuclein. Proc Natl Acad Sci USA 116:17963-17969. <https://doi.org/10.1073/pnas.19061241169>
23. Rasmussen MK, Mestre H, Nedergaard M (2018) The glymphatic pathway in neurological disorders. Lancet Neurol 17:1016-1024. [https://doi.org/10.1016/S1474-4422\(18\)30318-1](https://doi.org/10.1016/S1474-4422(18)30318-1)
24. Doehner J, Genoud C, Imhof C, Krstic D, Knuesel I (2012) Extrusion of misfolded and aggregated proteins—a protective strategy of aging neurons? Eur J Neurosci 35:1938-1950. <https://doi.org/10.1111/j.1460-9568.2012.08154.x>
25. Kocherhans S, Madhusudan A, Doehner J, Breu KS, Nitsch RM, Fritschy JM et al (2009) Reduced Reelin expression accelerates amyloid-beta plaque formation and tau pathology in transgenic Alzheimer's disease mice. J Neurosci 30:9228-9240. <https://doi.org/10.1523/JNEUROSCI.0418-10.2010>
26. Oddo S, Caccamo A, Shepherd JD, Murphy MP, Golde TE, Kaye R et al (2003) Tripletransgenic model of Alzheimer's disease with plaques and tangles: intracellular A β and synaptic dysfunction. Neuron

39:409–421. [https://doi.org/10.1016/s0896-6273\(03\)00434-3](https://doi.org/10.1016/s0896-6273(03)00434-3)

27. Brückner G, Brauer K, Härtig W, Wolff JR, Rickmann MJ, Derouiche A et al (1993) Perineuronal nets provide a polyanionic, glia-associated form of microenvironment around certain neurons in many parts in the rat brain. *Glia* 8:183-200. <https://doi.org/10.1002/glia.440080306>

28. Suttkus A, Holzer M, Morawski M, Arendt T (2016) The neuronal extracellular matrix restricts distribution and internalization of aggregated Tau-protein. *Neuroscience* 313:225-235. <https://doi.org/10.1016/j.neuroscience.2015.11.040>

29. Sorg BA, Berretta S, Blacktop JM, Fawcett JW, Kitagawa H, Kwok JC et al (2016) Casting a Wide Net: Role of Perineuronal Nets in Neural Plasticity. *J Neurosci* 36:11459-11468. <https://doi.org/10.1523/JNEUROSCI.2351-16.2016>

30. Mastrangelo MA, Bowers WJ (2008) Detailed immunohistochemical characterization of temporal and spatial progression of Alzheimer's disease-related pathologies in male triple-transgenic mice. *BMC Neurosci* 9:81. <https://doi.org/10.1186/1471-2202-9-81>

31. Härtig W, Saul A, Kacza J, Grosche J, Goldhammer S, Michalski et al (2014) Immunolesion-induced loss of cholinergic projection neurones promotes β -amyloidosis and tau hyperphosphorylation in the hippocampus of triple transgenic mice. *Neuropathol Appl Neurobiol* 40:106-120. <https://doi.org/10.1111/nan.12050>

32. [Hofstein R](#), Hesse G, [Shashoua VE](#) (1983) Proteins of the extracellular fluid of mouse brain: extraction and partial characterization. *J Neurochem* 40:1448-1455. <https://doi.org/10.1111/j.1471-4159.1983.tb13589.x>

33. Pulli B, Ali M, Forghani R, Schob S, Hsieh KL, Wojtkiewicz G, Linnoila JJ et al (2013) Measuring myeloperoxidase activity in biological samples. *PLoS One* 8:e67976. <https://doi.org/10.1371/journal.pone.0067976>

34. Ross GF, Ikegami M, Steinhilber W, Jobe AH (1999) Surfactant protein C in fetal and ventilated preterm rabbit lungs. *Am J Physiol* 277:L1104-1108. <https://doi.org/10.1152/ajplung.1999.277.6.L1104>

35. Kittler J, Illingworth J (1986) Minimum error thresholding. *Pattern Recognition* 19:41–47. [https://doi.org/10.1016/0031-3203\(86\)90030-0](https://doi.org/10.1016/0031-3203(86)90030-0)

36. Knuesel I, Nyffeler M, Mormède C, Muhia M, Meyer U, Pietropaolo S et al (2009) Age-related accumulation of Reelin in amyloid-like deposits. *Neurobiol Aging* 30:697-716. <https://doi.org/10.1016/j.neurobiolaging.2007.08.011>

37. Butkevich E, Härtig W, Nikolov M, Erck C, Grosche J, Urlaub H et al (2016) Phosphorylation of FEZ1 by Microtubule Affinity Regulating Kinases regulates its function in presynaptic protein trafficking. *Sci Rep* 6:26965. <https://doi.org/10.1038/srep26965>

38. Jucker M, Walker LC, Martin LJ, Kit CA, Kleinman HK, Ingram DK, Price DL (1992). Age-associated inclusions in normal and transgenic mouse brain. *Science* 255(5050):1443-5. doi: 10.1126/science.1542796
39. Jucker M, Walker LC, Kuo H, Tian M, Ingram DK (1994). Age-related fibrillar deposits in brains of C57BL/6 mice. A review of localization, staining characteristics, and strain specificity. *Mol Neurobiol.* 9(1-3):125-33. doi: 10.1007/BF02816112
40. Willander H, Hermansson E, Johansson J, Presto J (2011) BRICHOS domain associated with lung fibrosis, dementia and cancer—a chaperone that prevents amyloid fibril formation? *FEBS J* 278:3893-3904. <https://doi.org/10.1111/j.1742-4658.2011.08209.x>
41. Keller A, Eistetter HR, Voss T, Schäfer KP (1991) The pulmonary surfactant protein C (SP-C) precursor is a type II transmembrane protein. *Biochem J* 277 (Pt2):493-499. <https://doi.org/10.1042/bj277049343>
42. Hoe HS, Lee KJ, Carney RS, Lee J, Markova A, Lee JY et al (2009) Interaction of reelin with amyloid precursor protein promotes neurite outgrowth. *J Neurosci* 29:7459-7473. <https://doi.org/10.1523/JNEUROSCI.4872-08.2009>
43. Hoe HS, Tran TS, Matsuoka Y, Howell BW, Rebeck GW (2006) Dab1 and Reelin effects on APP and ApoE2 trafficking and processing. *J Biol Chem* 281:35176-35185. <https://doi.org/10.1074/jbc.M602162200>
44. Van Eldik LJ, Griffin WS (1994) S100 β expression in Alzheimer's disease: relation to neuropathology in brain regions. *Biochim Biophys Acta* 1223:398-403. [https://doi.org/10.1016/0167-4889\(94\)90101-5](https://doi.org/10.1016/0167-4889(94)90101-5)
45. Van Eldik LJ, Wainwright MS (2003) The Janus face of glial-derived S100B: beneficial and detrimental functions in the brain. *Restor Neurol Neurosci* 21:97–108.
46. Michetti F, D'Ambrosi N, Toesca A, Puglisi MA, Serrano A, Marchese E et al (2019) The S100B story: from biomarker to active factor in neural injury. *J Neurochem* 148:168-187. <https://doi.org/10.1111/jnc.14574>
47. Steiner J, Bernstein HG, Biellau H, Berndt A, Brisch R, Mawrin C, Keilhoff G et al (2007) Evidence for a wide extra-astrocytic distribution of S100B in human brain. *BMC Neurosci* 8:2. <https://doi.org/10.1186/1471-2202-8-2>
48. Cristóvão JS, Gomes CM (2019) S100 Proteins in Alzheimer's Disease. *Front Neurosci.* 2019;13:463. <https://doi.org/10.3389/fnins.2019.00463>
49. Celio MR, Spreafico R, De Biasi S, Vitarello-Zuccarello L (1998) Perineuronal nets: past and present. *Trends Neurosci* 21:510-515. [https://doi.org/10.1016/s0166-2236\(98\)01298-3](https://doi.org/10.1016/s0166-2236(98)01298-3)
50. Brauer K, Werner L, Leibnitz L (1982) Perineuronal nets of glia. *J Hirnforsch* 23:701-708

51. Härtig W, Brauer K, Brückner G (1992) Wisteria floribunda agglutinin-labelled nets surround parvalbumin-containing neurons. *Neuroreport* 3:869–872 <https://doi.org/10.1097/00001756-199210000-00012>.
52. Yamada J, Jinno S (2017) Molecular heterogeneity of aggrecan-based perineuronal nets around five subclasses of parvalbumin-expressing neurons in the mouse hippocampus. *J Comp Neurol* 525:1234-1249. <https://doi.org/10.1002/cne.24132>
53. Ueno H, Takao K, Suemitsu S, Murakami S, Kitamura N, Wani K et al (2018) Age-dependent and region-specific alteration of parvalbumin neurons and perineuronal nets in the mouse cerebral cortex. Age-dependent and region-specific alteration of parvalbumin neurons and perineuronal nets in the mouse cerebral cortex. *Neurochem Int* 112:59-70. <https://doi.org/10.1016/j.neuint.2017.11.001>
54. Härtig W, Derouiche A, Welt K, Brauer K, Grosche J, Mäder M et al (1999) Cortical neurons immunoreactive for the potassium channel Kv3.1b subunit are predominantly surrounded by perineuronal nets presumed as a buffering system for cations. *Brain Res* 842:15-29. [https://doi.org/10.1016/S0006-8993\(99\)01784-9](https://doi.org/10.1016/S0006-8993(99)01784-9)
55. Wingert JC, Sorg BA (2021) Impact of Perineuronal Nets on Electrophysiology of Parvalbumin Interneurons, Principal Neurons, and Brain Oscillations: A Review. *Front Synaptic Neurosci* 13:673210. <https://doi.org/10.3389/fnsyn.2021.673210>
56. Wegner F, Härtig W, Bringmann A, Grosche J, Wohlfarth K, Zuschratter W et al (2003) Diffuse perineuronal nets and modified pyramidal cells immunoreactive for glutamate and the GABA(A) receptor alpha1 subunit form a unique entity in rat cerebral cortex. *Exp Neurol* 184:705-714. [https://doi.org/10.1016/S0014-4886\(03\)00313-3](https://doi.org/10.1016/S0014-4886(03)00313-3)
57. Horn AKE, Horng A, Buresch N, Messoudi A, Härtig W (2018) Identification of Functional Cell Groups in the Abducens Nucleus of Monkey and Human by Perineuronal Nets and Choline Acetyltransferase Immunolabeling. *Front Neuroanat* 12:45. <https://doi.org/10.3389/fnana.2018.00045>
58. Irvine SF, Kwok JCF (2018) Perineuronal Nets in Spinal Motoneurons: Chondroitin Sulphate Proteoglycan around Alpha Motoneurons. *Int J Mol Sci* 19:1172. <https://doi.org/10.3390/ijms19041172>
59. Morawski M, Reinert T, Meyer-Klaucke W, Wagner FE, Tröger W, Reinert A et al (2015) Ion exchanger in the brain: Quantitative analysis of perineuronally fixed anionic binding sites suggests diffusion barriers with ion sorting properties. *Sci Rep* 5:16471. <https://doi.org/10.1038/srep16471>
60. Hockfield S, Kalb RG, Zaremba S, Fryer H (1990) Expression of neural correlates with the acquisition of mature neuronal properties in the mammalian brain. *Cold Spring Harb Symp Quant Biol* 155:505-514. <https://doi.org/10.1101/sqb.1990.055.01.049>

61. Bozzelli PL, Alaiyed S, Kim E, Villapol S, Conant K (2018) Proteolytic Remodeling of Perineuronal Nets: Effects on Synaptic Plasticity and Neuronal Population Dynamics. *Neural Plast* 2018:5735789. <https://doi.org/10.1155/2018/5735789>
62. Carstens KE, Phillips ML, Pozzo-Miller L, Weinberg RJ, Dudek SM (2016) Perineuronal Nets Suppress Plasticity of Excitatory Synapses on CA2 Pyramidal Neurons. *J Neurosci* 36:6312-6320. <https://doi.org/10.1523/JNEUROSCI.0245-16.2016>
63. Hayani H, Song I, Dityatev A (2018) Increased Excitability and Reduced Excitatory Synaptic Input Into Fast-Spiking CA2 Interneurons After Enzymatic Attenuation of Extracellular Matrix. *Front Cell Neurosci* 12:149. <https://doi.org/10.3389/fncel.2018.00149>
64. Lensjø KK, Christensen AC, Tennøe S, Fyhn M, Hafting T (2017) Differential Expression and Cell-Type Specificity of Perineuronal Nets in Hippocampus, Medial Entorhinal Cortex, and Visual Cortex Examined in the Rat and Mouse. *eNeuro* 4:ENEURO.0379-16.2017. <https://doi.org/10.1523/ENEURO.0379-16.2017>
65. Gogolla N, Caroni P, Lüthi A, Herry C (2009) Perineuronal nets protect fear erasure. *Science* 325:258–261. <https://doi.org/10.1126/science.1174146>
66. Tsien RY (2013) Very long-term memories may be stored in the pattern of holes in the perineuronal net. *Proc Natl Acad Sci USA* 110:12456–12461. <https://doi.org/10.1073/pnas.1310158110>
67. Lasek AW, Chen H, Chen WY (2018) Releasing Addiction Memories Trapped in Perineuronal Nets. *Trends Genet* 34:197-208. <https://doi.org/10.1016/j.tig.2017.12.004>
68. Paylor JW, Wendlandt E, Freeman TS, Greba Q, Marks WN, Howland JG et al (2018) Impaired Cognitive Function after Perineuronal Net Degradation in the Medial Prefrontal Cortex. *eNeuro* 5:e0253-18.2018. <https://doi.org/10.1523/ENEURO.0253-18.2018>
69. McRae PA, Baranov E, Rogers SL, Porter BE (2012) Persistent decrease in multiple components of the perineuronal net following status epilepticus. *Eur J Neurosci* 36:3471-3482. <https://doi.org/10.1111/j.1460-9568.2012.08268.x>
70. Rankin-Gee EK, McRae PA, Baranov E, Rogers S, Wandrey L, Porter BE (2015) Perineuronal net degradation in epilepsy. *Epilepsia* 56:1124-1133. <https://doi.org/10.1111/epi.13026>
71. Slaker ML, Jorgensen ET, Hegarty DM, Liu X, Kong Y et al (2018) Cocaine Exposure Modulates Perineuronal Nets and Synaptic Excitability of Fast-Spiking Interneurons in the Medial Prefrontal Cortex. *eNeuro* 5:ENEURO.0221-18.2018. <https://doi.org/10.1523/ENEURO.0221-18.2018>
72. Berretta S, Pantazopoulos H, Markota M, Brown C, Batzianouli ET (2015) Losing the sugar coating: Potential impact of perineuronal net abnormalities on interneurons in schizophrenia. *Schizophr Res* 167:18-27. <https://doi.org/10.1016/j.schres.2014.12.040>

73. Forostyak S, Homola A, Turnovcova K, Svitil P, Jendelova P, Sykova E (2014) Intrathecal delivery of mesenchymal stromal cells protects the structure of altered perineuronal nets in SOD1 rats and amends the course of ALS. *Stem Cells*. 32:3163-3172. <https://doi.org/10.1002/stem.1812>
74. Härtig W, Mages B, Aleithe S, Altmann S, Barthel H, et al. (2017) Damaged Neocortical Perineuronal Nets Due to Experimental Focal Cerebral Ischemia in Mice, Rats and Sheep. *Front Integr Neurosci* 11:15. <https://doi.org/10.3389/fnint.2017.00015>
75. Dzyubenko E, Manrique-Castano D, Kleinschnitz C, Faissner A, Hermann DM (2018) Topological remodeling of cortical perineuronal nets in focal cerebral ischemia and mild hypoperfusion. *Matrix Biol* 74:121-132. <https://doi.org/10.1016/j.matbio.2018.08.001>
76. Brückner G, Hausen D, Härtig W, Drlicek M, Arendt T, Brauer K (1999) Cortical areas abundant in extracellular matrix chondroitin sulphate proteoglycans are less affected by cytoskeletal changes in Alzheimer's disease. *Neuroscience* 92:791–805. [https://doi.org/10.1016/s0306-4522\(99\)00071-8](https://doi.org/10.1016/s0306-4522(99)00071-8)
77. Suttikus A, Morawski M, Arendt T (2016) Protective properties of neural extracellular matrix. *Mol Neurobiol* 53:73-82. <https://doi.org/10.1007/s12035-014-8990-4>
78. Morawski M, Brückner MK, Riederer P, Brückner G, Arendt T (2004) Perineuronal nets potentially protect against oxidative stress. *Exp Neurol* 188:309–315. <https://doi.org/10.1016/j.expneurol.2004.04.017>
79. Cabungcal JH, Steullet P, Morishita H, Kraftsik R, Cuenod M, Hensch TK et al (2013) Perineuronal nets protect fast-spiking interneurons against oxidative stress. *Proc Natl Acad Sci USA* 110:9130–9135. <https://doi.org/10.1073/pnas.1300454110>
80. Fawcett JW, Oohashi T, Pizzorusso T (2019) The roles of perineuronal nets and the perinodal extracellular matrix in neuronal function. *Nat Rev Neurosci* 20:451-465. <https://doi.org/10.1038/s41583-019-0196-3>
81. Reichelt AC, Hare DJ, Bussey TJ, Saksida LM. (2019) Perineuronal Nets: Plasticity, Protection, and Therapeutic Potential. *Trends Neurosci* 42:458-470. <https://doi.org/10.1016/j.tins.2019.04.003>
82. Testa D, Prochiantz A, Di Nardo AA (2019) Perineuronal nets in brain physiology and disease. *Semin Cell Dev Biol* 89:125-135. <https://doi.org/10.1016/j.semcdb.2018.09.011>
83. Wen TH, Binder DK, Ethell IM, Razak KA (2018) The Perineuronal 'Safety' Net? Perineuronal Net Abnormalities in Neurological Disorders. *Front Mol Neurosci* 11:270. <https://doi.org/10.3389/fnmol.2018.00270>
84. de Winter F, Kwok JC, Fawcett JW, Vo TT, Carulli D, Verhaagen J (2016) The Chemorepulsive Protein Semaphorin 3A and Perineuronal Net-Mediated Plasticity. *Neural Plast* 2016:3679545. <https://doi.org/10.1155/2016/3679545>

85. Carulli D, Verhaagen J (2021) An Extracellular Perspective on CNS Maturation: Perineuronal Nets and the Control of Plasticity. *Int J Mol Sci* 22:2434. <https://doi.org/10.3390/ijms22052434>
86. Van't Spijker HM, Rowlands D, Rossier J, Haenzi B, Fawcett JW, Kwok JCF (2019) Neuronal Pentraxin 2 Binds PNNs and Enhances PNN Formation. *Neural Plast* 2019:6804575. <https://doi.org/10.1155/2019/6804575>
87. Beurdeley M, Spatazza J, Lee HH, Sugiyama S, Bernard C, Di Nardo AA et al (2012) [Otx2 binding to perineuronal nets persistently regulates plasticity in the mature visual cortex](#). *J Neurosci* 32:9429-9437. <https://doi.org/10.1523/JNEUROSCI.0394-12.2012>
88. Hou X., Yoshioka N, Tsukano H, Sakai A, Miyata S, Watanabe Y et al (2017) Chondroitin Sulfate Is Required for Onset and Offset of Critical Period Plasticity in Visual Cortex. *Sci Rep* 7:12646. <https://doi.org/10.1038/s41598-017-04007-x>
89. Mulugeta S, Beers MF (2003) Processing of surfactant protein C requires a type II transmembrane topology directed by juxtamembrane positively charged residues. *J Biol Chem* 278:47979-47986. <https://doi.org/10.1074/jbc.M308210200>

Tables

Table 1. Overview of investigated mice

	Immunofluorescence labelling		Enzyme-linked immunoassays	
	WT	3xTg	WT	3xTg
3 months	10	5	3	10
6 months	4	8	8	6
12 months	6	7	6	6
16 months	6	6	6	7
24 months	6	6	5	

Table 2. Double fluorescence labelling combined with the Cy2-staining of SP-C

First primary antibodies	Fluorochromated secondary antibodies	Second primary antibodies or lectins	Fluorochromated secondary antibodies and streptavidin conjugates
goat-anti-AQP4 (1:1000; Santa Cruz, Heidelberg)	Cy3-donkey-anti-goat IgG	biotinylated STL (20µg/ml; Vector, Burlingame, CA, USA)	Cy5-streptavidin
mouse-anti-oligodendroglia (RIP; 1:400; Merck Millipore, Billerica, CA, USA)	Cy3-donkey-anti-mouse IgG	guinea pig-anti-GFAP (1:200; Synaptic Systems, Göttingen, Germany)	Cy5-donkey-anti-guinea pig IgG
guinea pig-anti-Iba (1:100; Synaptic Systems)	Cy3-donkey-anti-guinea pig IgG	mouse-anti-S100β (1:50; Sigma, Taufkirchen, Germany)	Cy5-donkey-anti-mouse IgG
Cy3-mouse-anti-GFAP (1:250, Sigma)		guinea pig-anti-S100β (1:200; Synaptic Systems)	Cy5-donkey-anti-guinea pig IgG
guinea pig-anti-S100β (1:200; Synaptic Systems)	Cy3-donkey-anti-guinea pig IgG	mouse-anti-CNP (1:200; Synaptic Systems)	Cy5-donkey-anti-mouse IgG
guinea pig-anti-NeuN (1:300; Synaptic Systems)	Cy3-donkey-anti-guinea pig IgG	mouse-anti-S100β (1:50; Sigma)	Cy5-donkey-anti-mouse IgG
biotinylated WFA (10 µg/ml; Vector)	Cy3-streptavidin	guinea pig anti-parvalbumin (1:200; Synaptic Systems)	Cy5-donkey-anti-guinea pig IgG
mouse-anti-aggrecan (1:40, Acris, Herford, Germany)	Cy3-donkey-anti-rabbit IgG	biotinylated WFA (15 µg/ml; Vector)	Cy5-streptavidin
goat-anti-HAPLN1 (1:100; R&D Systems, Minneapolis, USA)	Cy3-donkey-anti-goat IgG	Biotinylated WFA (15µg/ml; Vector)	Cy5-streptavidin
guinea pig-anti-S100β (1:300; Synaptic Systems)	Cy3-donkey-anti-guinea pig IgG	biotinylated WFA (15 µg/ml; Vector)	Cy5-streptavidin
goat-anti-neurocan (1:400; R&D Systems, Minneapolis, MN, USA)	Cy3-donkey-anti-goat IgG	biotinylated WFA (15 µg/ml; Vector)	Cy5-streptavidin
guinea pig-anti-VGAT (1:500; Synaptic Systems)	Cy3-donkey-anti-guinea pig IgG	biotinylated WFA (15 µg/ml; Vector)	Cy5-streptavidin
guinea pig-anti-VGLUT1(1:1000; Synaptic Systems)	Cy3-donkey-anti-guinea pig IgG	biotinylated WFA (15 µg/ml; Vector)	Cy5-streptavidin
guinea pig-anti-VGLUT2 (1:500; Synaptic Systems)	Cy3-donkey-anti-guinea pig IgG	biotinylated WFA (15 µg/ml; Vector)	Cy5-streptavidin
guinea pig-anti-VGLUT2	Cy3-donkey-anti-	biotinylated mouse-	Cy5-streptavidin

(1:500; Synaptic Systems)	guinea pig IgG	anti-A β ₁₈₋₂₃ (4G8, 1:50)	
guinea pig-anti-VGLUT2 (1:500; Synaptic Systems)	Cy3-donkey-anti- guinea pig IgG	biotinylated anti- phospho-tau (p202 + p205, AT8, 1:50)	Cy5-streptavidin
mouse-anti-Reelin (1:200; Merck Millipore)	Cy3-donkey-anti- mouse IgG	goat-anti-AQP4 (1:500; Santa Cruz, Heidelberg, Germany)	AlexaFluor647-donkey- anti-goat IgG

Due to technical limitations, Table 3 is only available as a download in the Supplemental Files section.

Figures

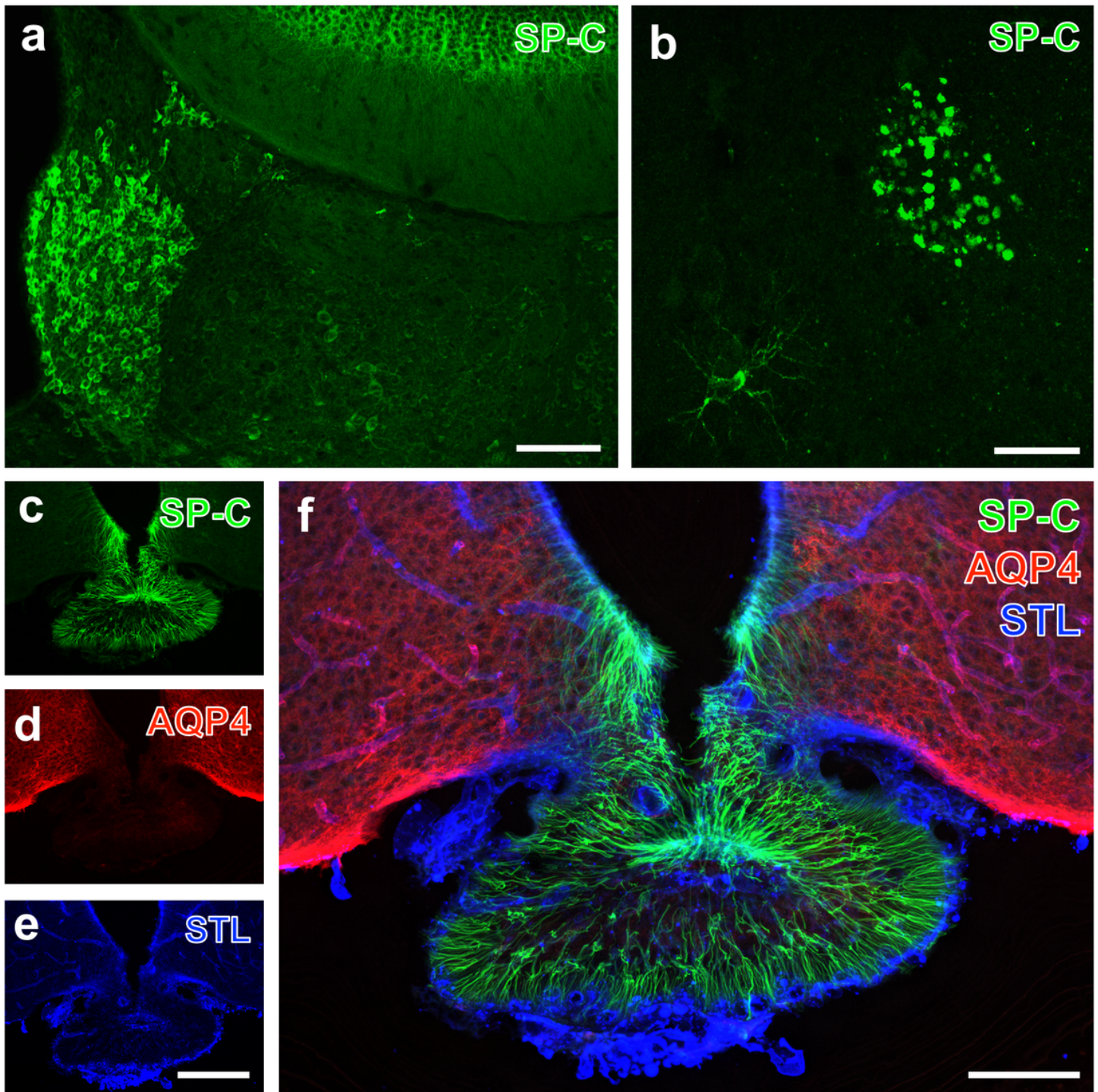


Figure 1

Multifaceted green fluorescent Cy2-immunolabelling of SP-C in the brain. a The medial habenula displays heavily stained, round cells as shown here for a 3-month-old 3xTg mouse. b Confocal laser scanning reveals in the hippocampus of a two-year-old WT mouse both a ramified cell with glial appearance and a cluster with dot-like deposits. c The infundibulum of a 6-month-old WT mouse shows numerous SP-C-ir fibrous processes contacting the ependymal border. d Counterstaining of AQP4 (Cy3, red) is widely absent in the infundibulum but strong in the adjacent tissue and especially its vasculature.

Concomitantly applied STL visualized by Cy5-streptavidin (colour-coded in blue) detects both the same vessels and the ependyma of the infundibulum. f The merged staining patterns primarily clarify complementary localisation of SP-C and AQP4. Bars: a = 100 μ m, b = 25 μ m, e = 200 μ m, f = 200 μ m (also valid for c-d).

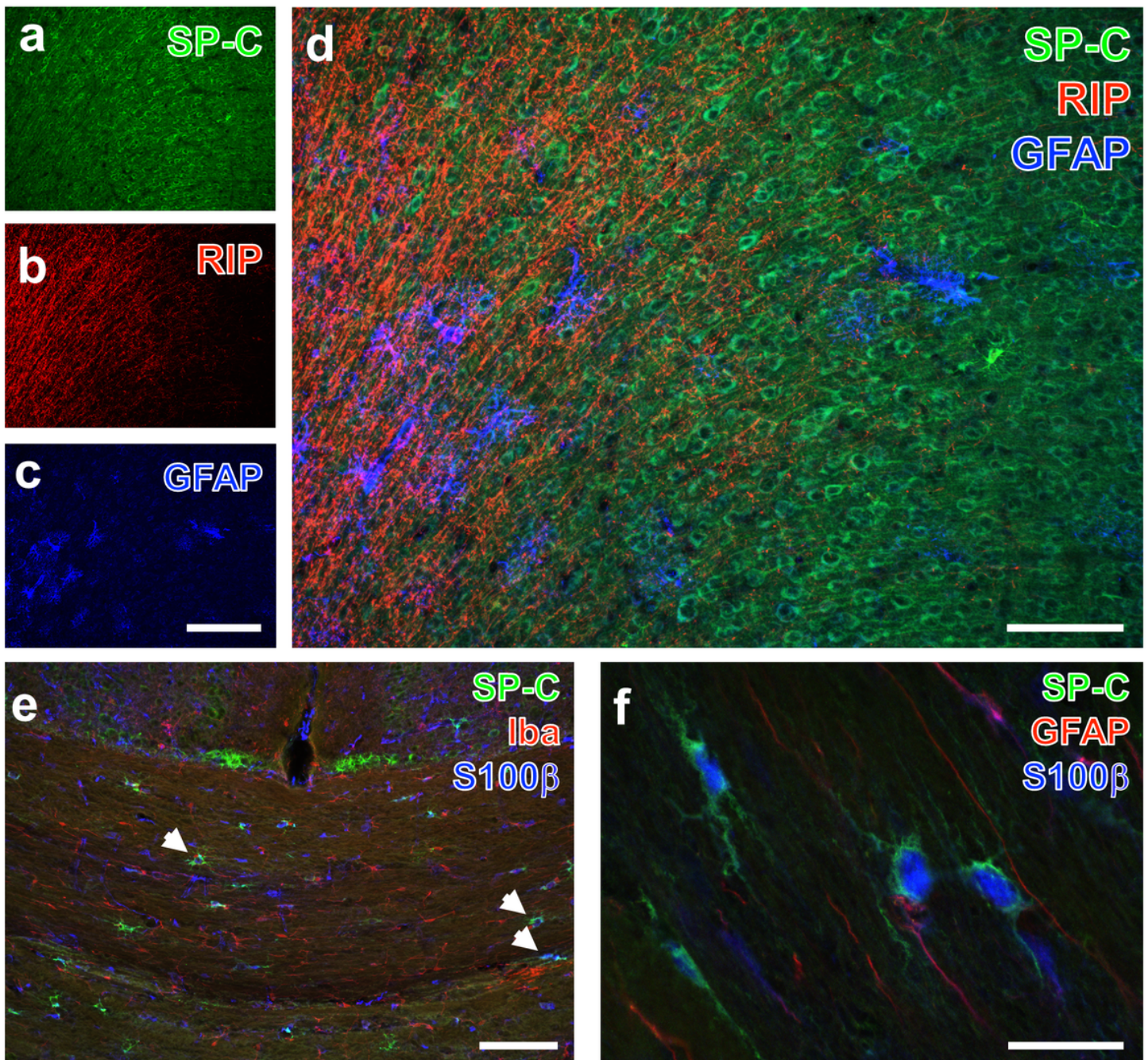


Figure 2

Lacking SP-C-ir in GFAP-immunopositive astroglia, oligodendroglial and microglial structures, but co-occurrence in S100 β -containing astrocytes from 3-month-old WT mice. a In the cingular cortex, SP-C-ir (Cy2, green) is predominantly visible in the rim of apparently neuronal cells and their proximal dendrites b In parallel, a fine network of different fibres is revealed by the oligodendroglia-specific antibody RIP (Cy3,

red). c The concomitant Cy5-staining of GFAP visualises several fibrous astrocytes colour-coded in blue. d Merge of the complementary staining patterns. (e) Double staining of SP-C-ir (Cy2, green) and S100 β (Cy5, blue) combined with detection of separately located Iba-immunopositive microglia (Cy3, red) in the corpus callosum. The overlay of all three staining patterns clearly reveals astrocytes containing apparently both S100 β and SP-C (arrows). f A confocal image of a representative triple staining for SP-C (green), S100 β (blue) and GFAP (red) clearly demonstrated that such GFAP-immunonegative astrocytes in the corpus callosum display S100-ir in the cytoplasm and SP-C in the surrounding rim. Bars: a,b, c, g, e = 200 μ m, d = 100 μ m, f = 25 μ m.

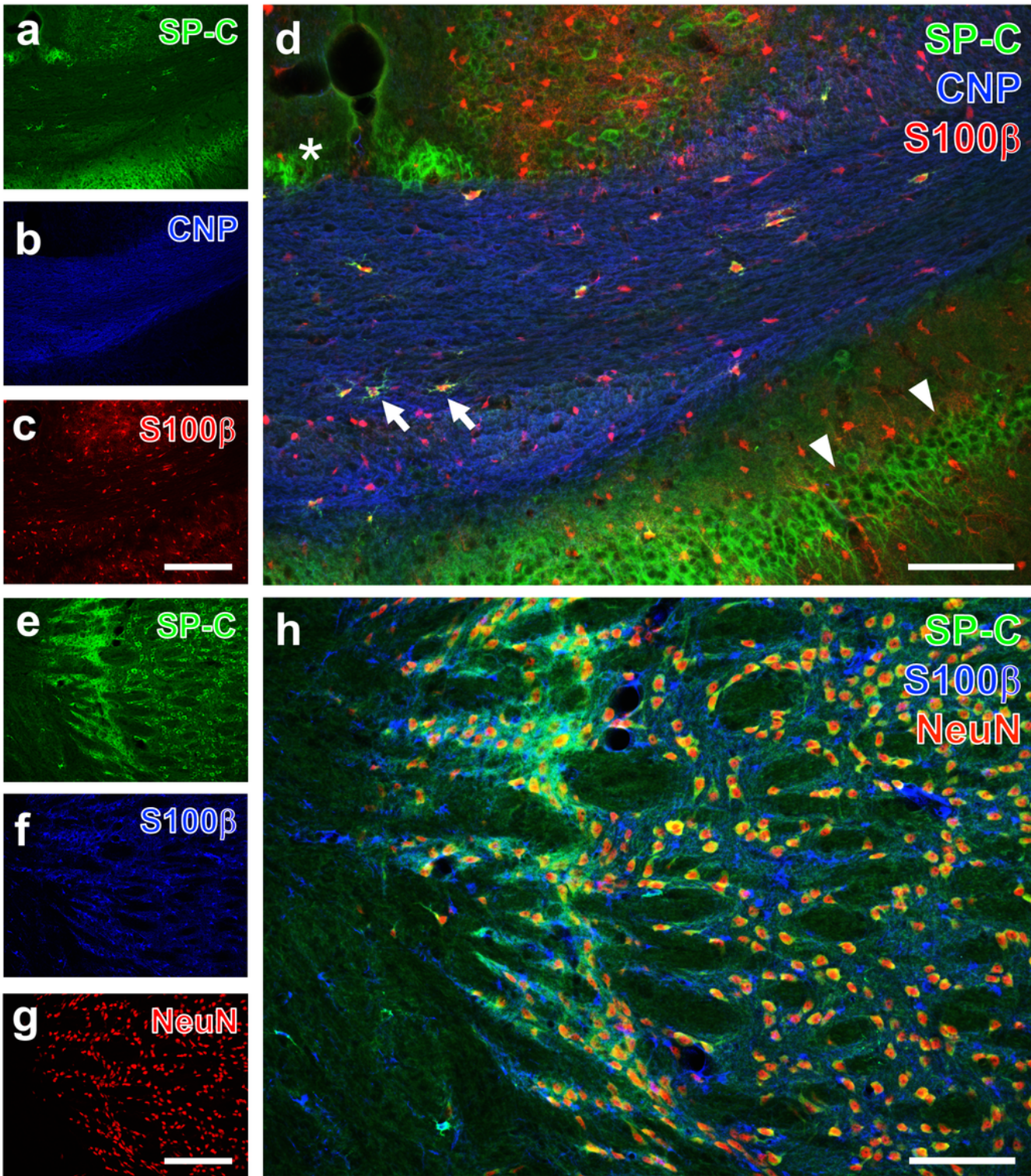


Figure 3

SP-C-ir in S100 β -expressing astrocytes and neurons from 3-month-old WT mice. a SP-C immunolabelling of ramified cells in the corpus callosum that is marked in b by its CNP-ir (Cy5, blue), combined in c with the detection of an astroglial subset based on guinea pig-anti-S100 β (Cy3, red). d The merging of single channels elucidates astrocytes double-positive for SP-C and S100 β (arrows) and that solely SP-C marks the indusium griseum (asterisk) and the granular layer of the hippocampal CA1 region (arrowheads). e

SP-C-ir appears strong in the nucleus reticularis thalami (NRT) and moderate in the ventral pallidum. Additionally, both nuclei display numerous cells immunopositive for S100 β (in f) and b NeuN (in g). The merge of staining patterns in h reveals the close vicinity of all three markers. Bars: c,g = 200 μ m (also valid for a,b,e,f), d,h = 100 μ m,

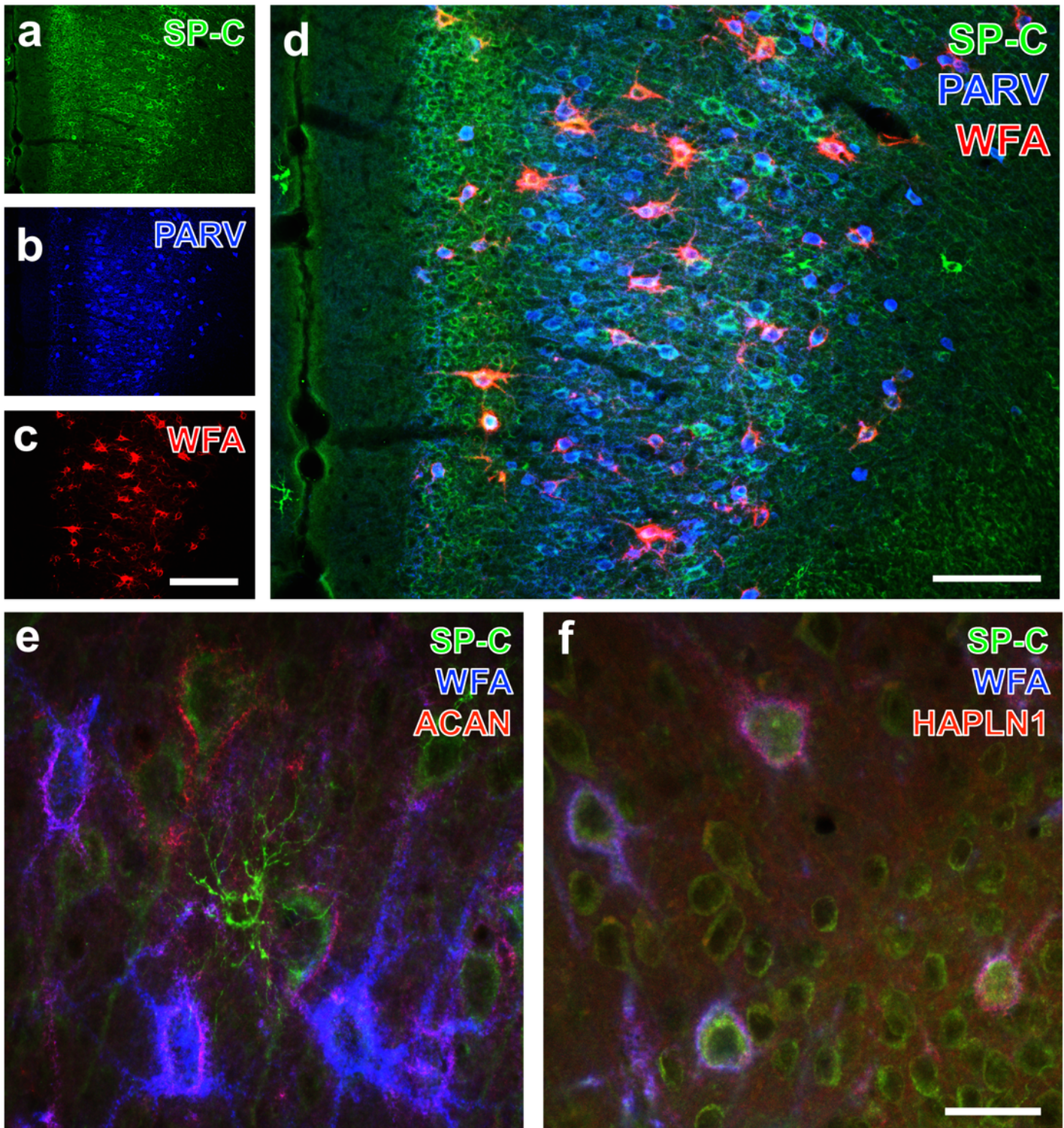


Figure 4

Co-occurrence of SP-C-ir, parvalbumin (PARV)-expressing neurons and PNs in the retrosplenial cortex from young WT mice. a SP-C-ir outlines the rim of numerous neurons and their proximal dendrites. In addition, stronger stained astroglial cells with fine processes are visible for instance at the border of both hemispheres. Nearly all neocortical layers contain concomitantly detected a PARV-immunopositive neurons (Cy5, blue) and b PNs labelled by biotinylated WFA and subsequently applied Cy3-streptavidin (red). d The overlay of all staining patterns demonstrates numerous PARV- and SP-C-ir nerve cells which are frequently ensheathed by PNs. In e, Z-stacks of confocal images elucidate at higher magnification a representative astrocyte and neurons combined with the detection of WFA-binding sites (Cy5, blue) and aggrecan (ACAN)-ir (Cy3) in PNs. Note the purple appearance of components displaying both net markers and their close vicinity to SP-C-ir. f Additionally, a confocal image exemplifies the triple labelling of SP-C (green), WFA (blue) and HAPLN1 (red) as further net component. Neuronal SP-C-ir are ensheathed by PNs with predominant HAPLN1-ir (red) and WFA/HAPLN1-double-stained nets appearing pink, Bars: c = 200 μm (also valid for a,b), d = 100 μm , e,f = 25 μm .

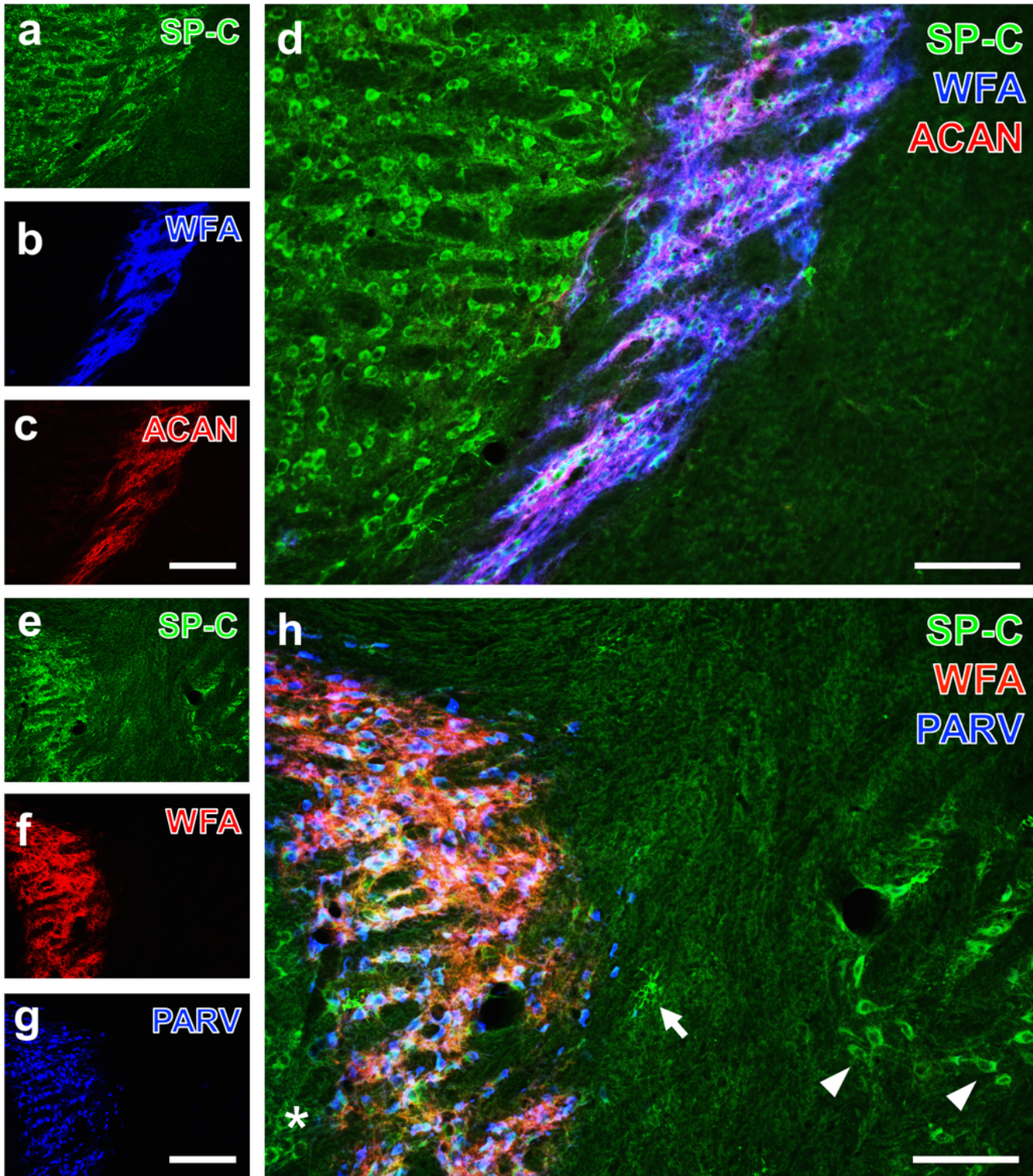


Figure 5

Associated SP-C-ir, PN and PARV-containing neurons in the nucleus reticularis thalami (NRT) from 3-month-old WT mice. a Densely packed SP-C-ir cells are observed in the NRT and the adjoining ventral pallidum. The latter is devoid of the net markers WFA (blue) in b and aggrecan (ACAN, red) in c, whereas the NRT is selectively visualised by a carpet-like staining of WFA and ACAN. d Merged staining patterns reveal co-occurring SP-C-ir and PN selectively in the NRT. e More laterally, neuronal SP-C-ir becomes

visible both in NRT and in the globus pallidus. Restricted to the NRT remain in f WFA-stained PN (Cy3, red) and in g PARV-ir neurons (Cy5, blue). h The overlay of green, red and blue fluorescence signals elucidates their allocation in the NRT highlighted by structures appearing white, whereas both ventral pallidum (asterisk) and caudate putamen (arrows) are solely visible by green SP-C immunolabelling. Bars: c, g = 200 μ m (also valid for a, b, e, f), d, h = 100 μ m.

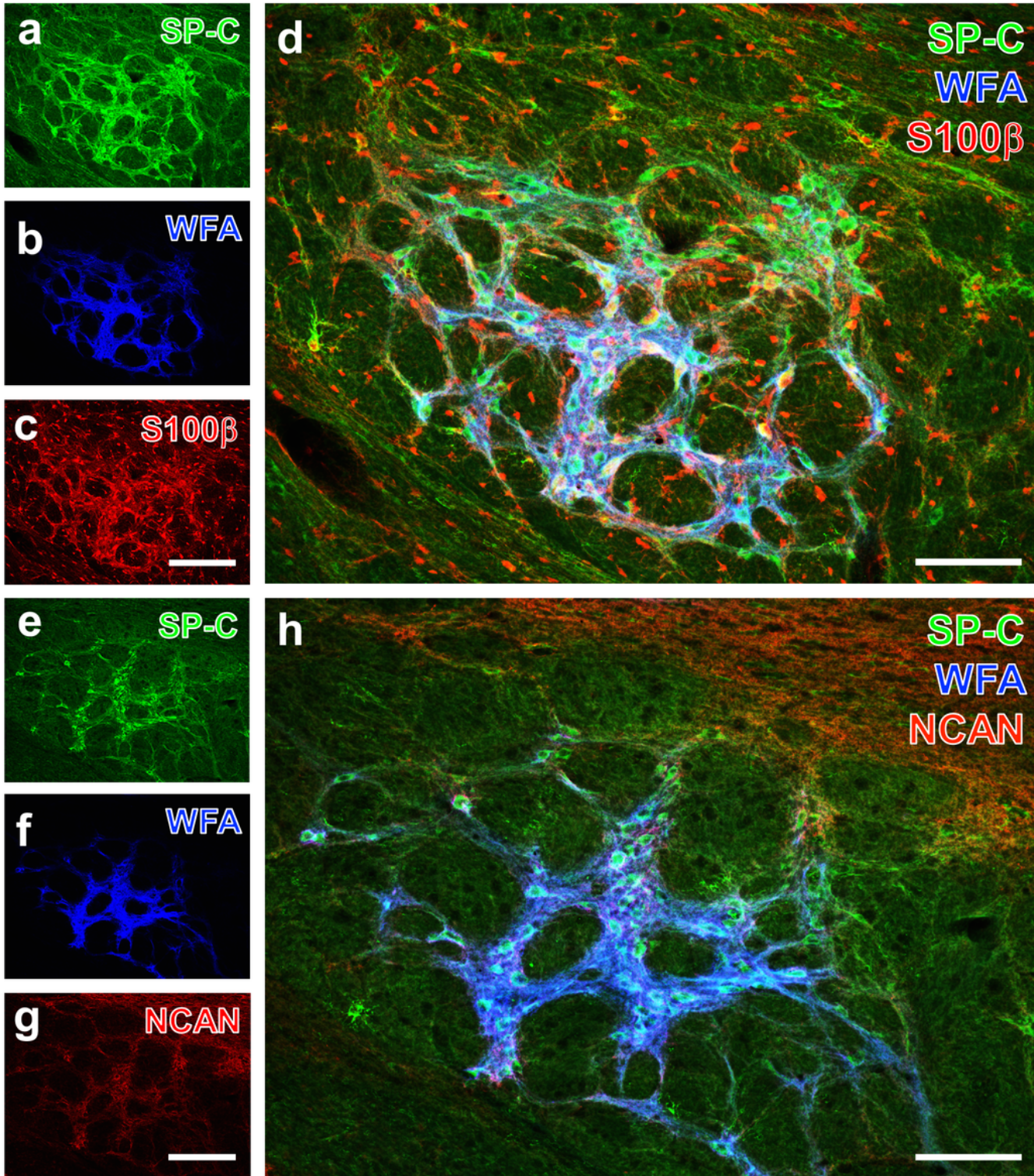


Figure 6

Co-occurrence of SP-C, PNs and S100 β in the lateral hypothalamic area (LHA) from 3-month-old WT mice. In this nucleus, numerous cells and their ensheathment are selectively revealed in a by SP-C ir (Cy2, green) and in b by WFA staining (Cy5, blue). c Concomitantly visualised S100 β -ir is found also in the surrounding tissue d The merged staining patterns show nearly congruent staining of all three markers in the LHA. Additional triple staining of the LHA combines the detection of SP-C-ir (in e) and WFA-binding sites (in f) as above with g the immunolabelling of the net component neurocan (NCAN, Cy3, red). h The overlay elucidates that the PNs in the LHA appear stronger stained by WFA than by NCAN and are frequently located in close vicinity to SP-C-ir neuronal structures. Bars: c,g = 200 μ m (also valid for a,b,e,f), d,h = 100 μ m.

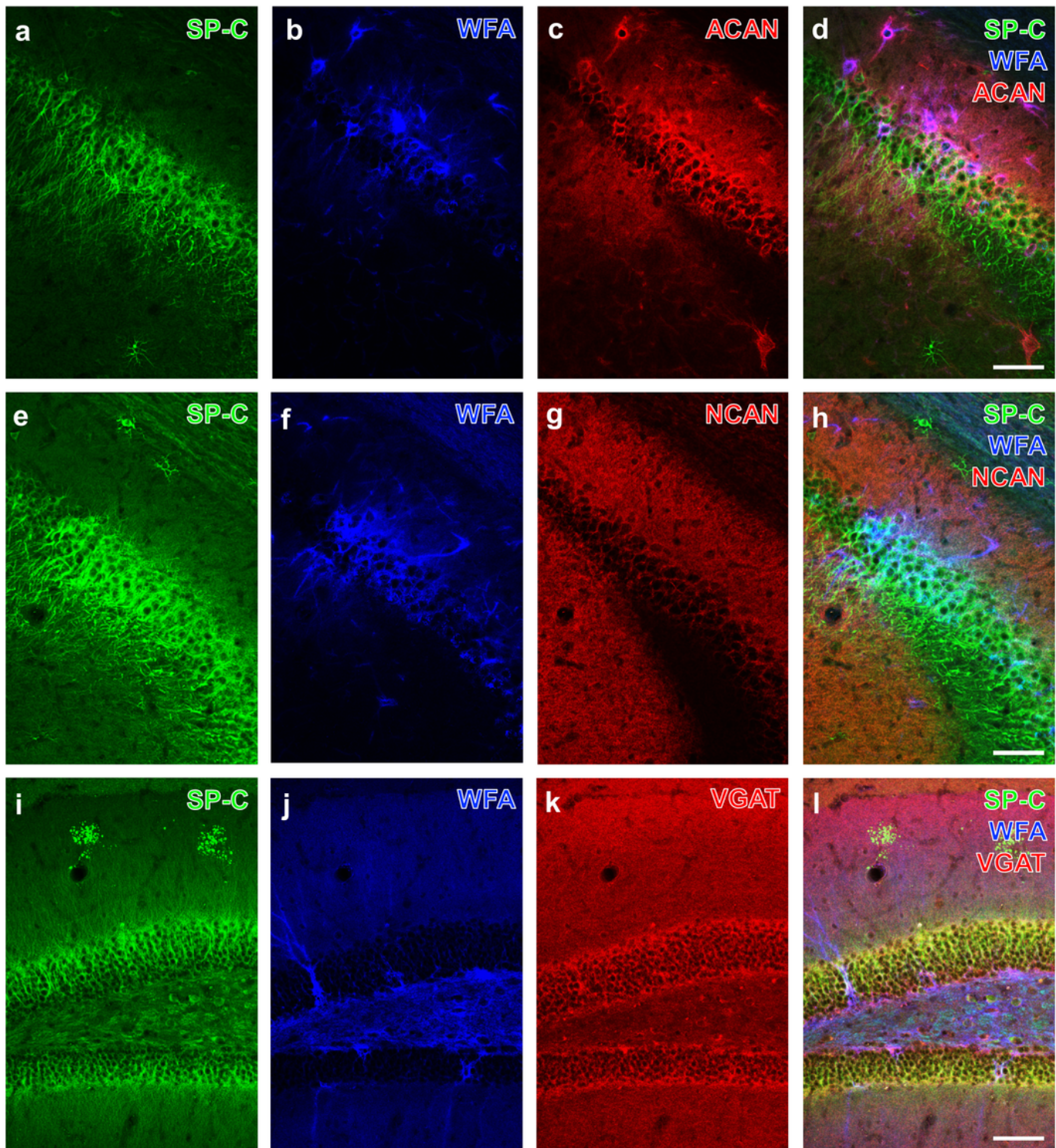


Figure 7

Hippocampal SP-C/WFA double staining combined with the immunodetection of aggrecan (ACAN), neurocan (NCAN) and VGAT including the border between CA1 and CA2 in WT mice with 6 months (a-d) as well as 24 months of age (e-h) and in the dentate gyrus in a very old animal (i-l). The simultaneous visualisation of SP-C, WFA and ACAN in d demonstrates for the CA2 region numerous heavily WFA/ACAN double-stained PN (appearing purple) and the allocation of SP-C-ir cells and WFA-binding sites (yellow).

Additionally, outside PNs the adjacent neuropil displays red immunolabelling for ACAN (Fig. 7c,d) and NCAN (Fig. 7g,h). i The gyrus dentatus is marked by a moderate cellular SP-C staining, while the stratum lacunosum-moleculare shows two clusters of dots. j The latter are devoid of WFA-binding sites while the gyrus dentatus is equipped with several PNs partly comprising long dendritic processes. k,l VGAT-ir contours the cellular layers, but is absent in the SP-C-containing dots. Bar d,h,l = 75 μ m (also valid for a-c,e-g,i-k).

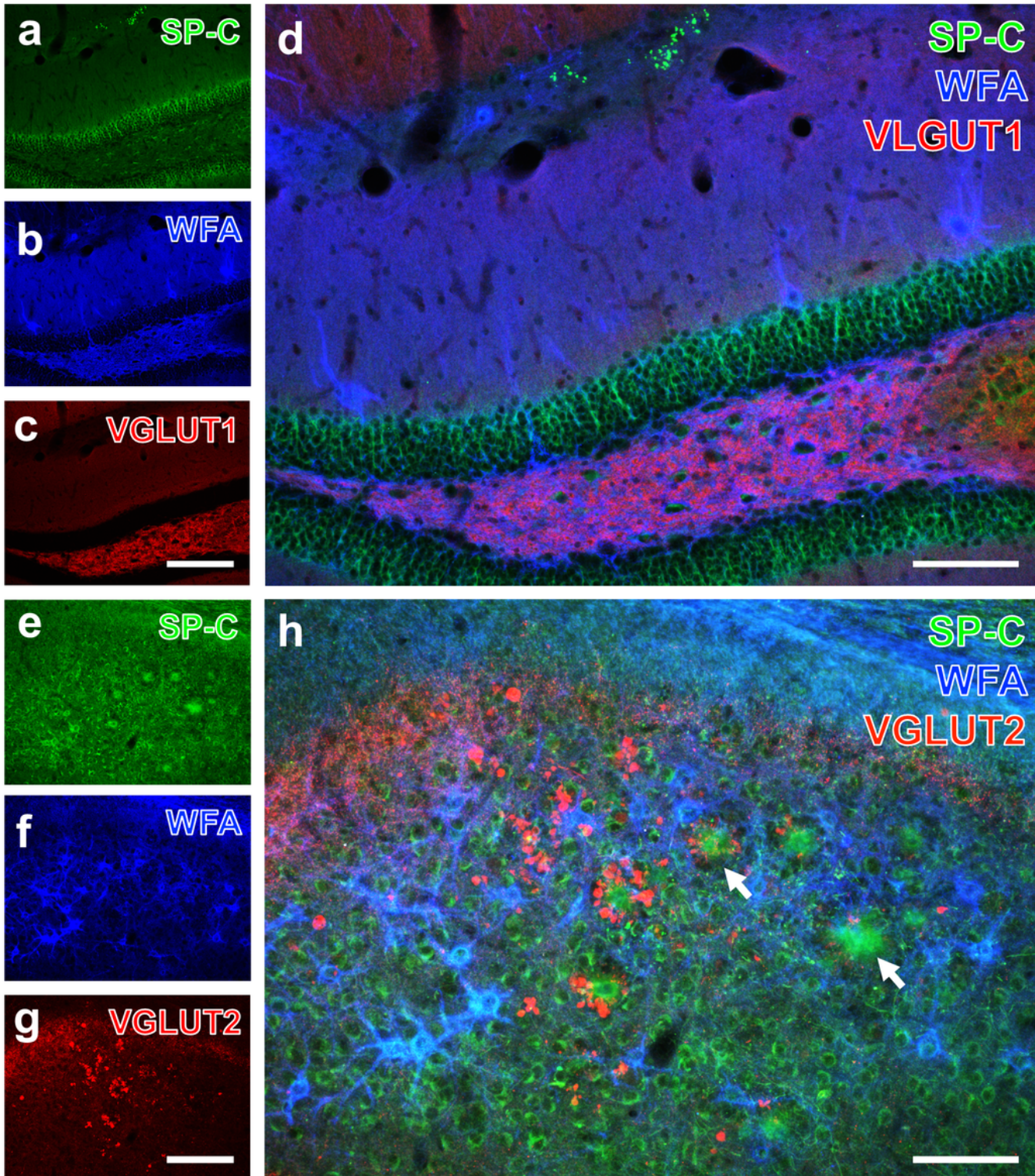


Figure 8

Combined fluorescence staining of SP-C and PNs and VGLUT1 (a-d) as well as VGLUT2 (e-h) in the hippocampus of aged mice. a-d CA1 region and dentate gyrus from a 22-month-old WT mouse, in a with SP-C-immunolabelled clusters of dots in the stratum lacunosum-moleculare and cellular structures in the gyrus dentatus which displays in b PNs with strongly WFA-stained dendrites (Cy5, blue). Concomitantly, c demonstrates VGLUT1-ir fibres (Cy3, red) predominantly in the hilus. d The overlay of staining patterns clearly shows the lacking allocation of VGLUT1 and both PNs and SP-C-immunopositive structures. e-h Subiculum from a 22-month-old 3xTg mouse, in e with SP-C-ir also indicating senile plaques, whereas f demonstrates several PNs heavily stained with WFA (Cy5, blue) and g displays in adjacent areas numerous deposits consisting of clearly contoured granules. d The overlay elucidates largely complementary staining patterns for the three markers. Bars: c,g = 200 μm (also valid for a,b,e,f), d,h = 100 μm .

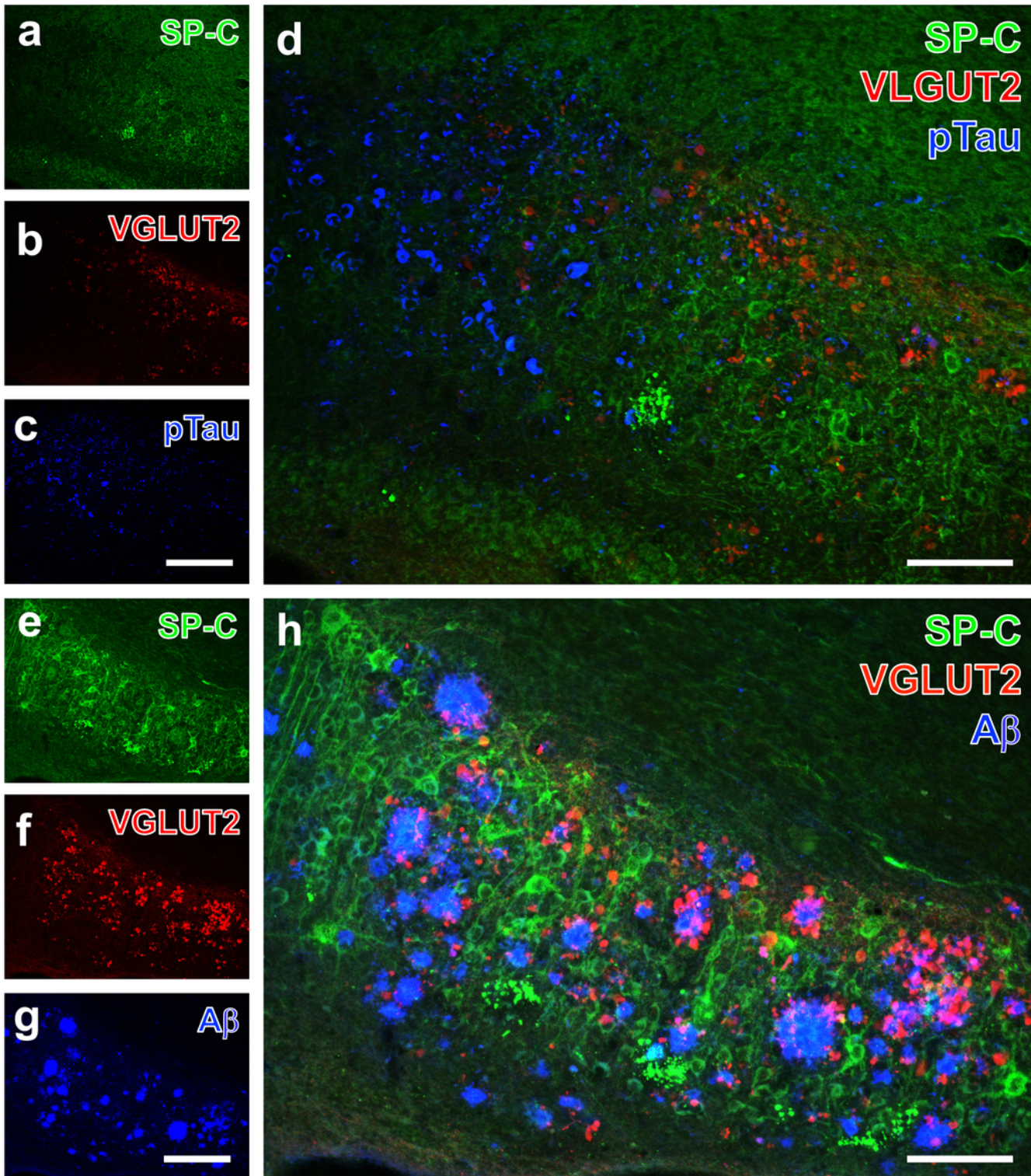


Figure 9

Differently composed age-dependently occurring hippocampal deposits. Double immunofluorescence of SP-C (Cy2, green) and VGLUT2 (Cy3, red) combined with the detection of (a-d) phospho-tau or (e-h) A β (both Cy5, colour-coded in blue) in the subiculum from 22-month-old 3xTg mice. a SP-C immunolabelling depicts single dots and a larger cluster of numerous dots as well as cellular structures. b Separately, VGLUT2-ir is predominantly seen near dots with frequently larger diameters. c The counterstaining of

hyperphosphorylated protein tau (phospho-tau) with biotinylated AT8 and Cy5-tagged streptavidin detects many deposits, partly with cellular appearance. d The overlay without any mixed colours clarifies the complete separation of the different deposited proteins. e Borders of the subiculum are filled with several clusters of dots as well as numerous SP-C-immunopositive cells. f Strong VGLUT2-ir in this region is largely confined to obviously different and mostly clustered dots with frequent larger diameters. g In close vicinity, the subiculum displays many A β -containing plaques, whereas adjoining structures are devoid of such deposits. h The overlay shows the allocation of the detected deposits, especially of A β and VGLUT-ir, whereas the SP-C-ir in dots and cells with frequently long processes appear neatly separated. Bars: c,g= 200 μ m (also valid for a,b,e,f), d,h = 100 μ m.

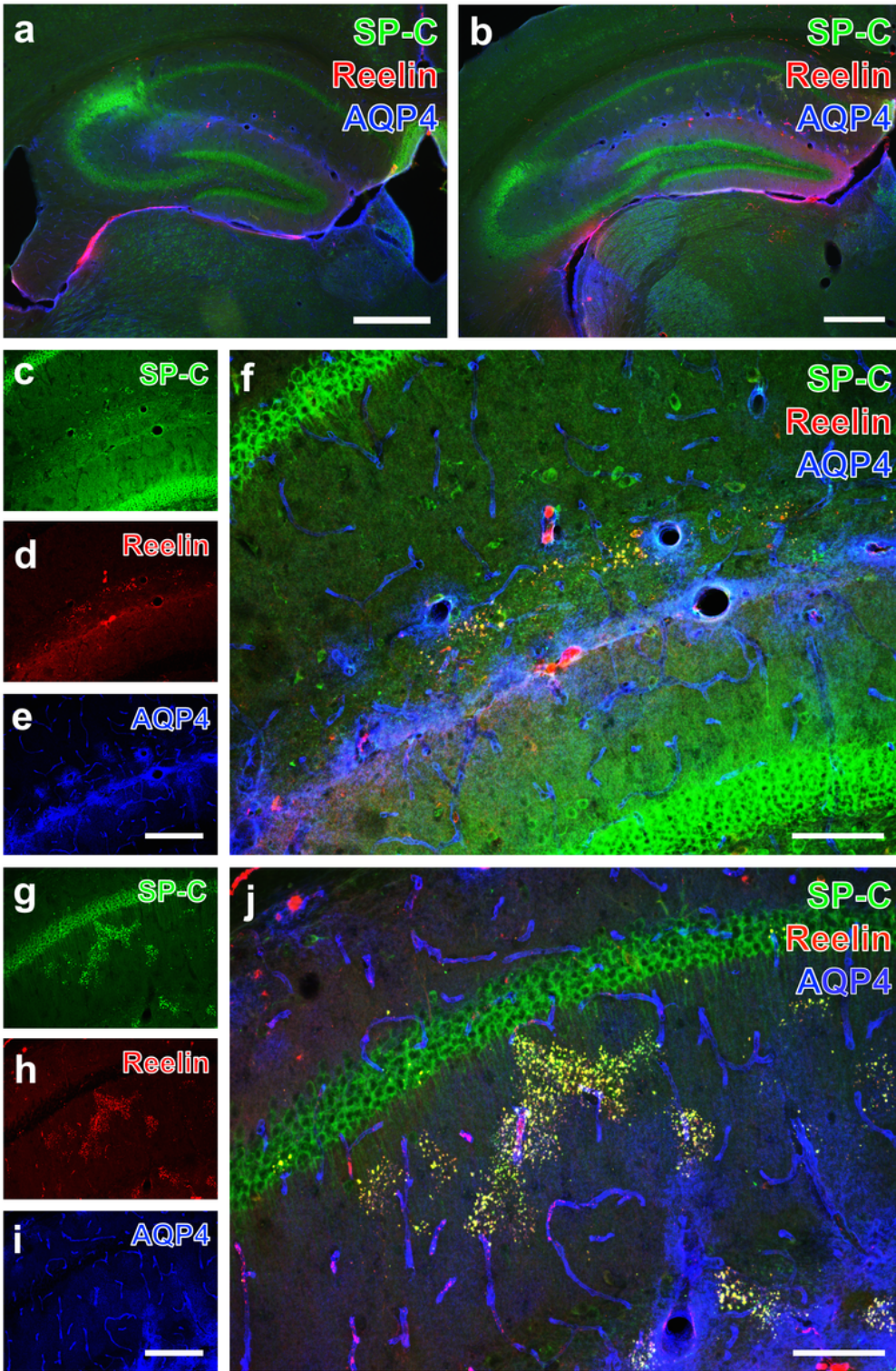


Figure 10

Age-dependently occurring clusters of SP-C- and Reelin-ir hippocampal dots and allocated AQP4-ir. 3-month-old (a,c-f) versus 16-month-old (b,g-j) 3xTg-mice at lower magnification (a,b) and with higher resolution (c-j). a SP-C immunolabelling (Cy2, green) primarily reveals a demarcation of the granular layers in the more rostral hippocampus with the heaviest staining in the CA2 area, a clearly marked indusium griseum and as strongest labelled neocortical areas the retrosplenial and cingular cortices.

Predominant Reelin-ir (Cy3, red) is exclusively visible at the vascular borders, whereas immunosignals for AQP4 (Cy5, blue) are dominating in the fissura hippocampalis and the lateral habenula. b The more caudally located hippocampus in an aged animal shows similar distribution patterns, but also several clusters of SP-C dots in the stratum radiatum and stratum oriens. c At higher magnification of the SP-C-ir in the young mouse, the CA1 region exhibits densely packed granular cells including their processes as well as some additional loosely distributed, faintly stained cells and dots. d Reelin immunolabelling of dots and a few cells in the fissura hippocampalis is more prominent, but it is absent in the granular layers which in e are also devoid of AQP4 immunosignals. AQP4-ir astroglial endfeet clearly reveal vessels. This marker appears strongest in the fuzzy- surroundings of perpendicularly cut vessels. f The overlay demonstrates that most dots are immunopositive for both SP-C and Reelin and appear yellowish, but some dots remain mono-labelled for Reelin. g At higher magnification, cellular SP-C-ir in the pyramidal layer from the aged triple-transgenic animal is largely the same as in c showing a hippocampal frame from a 3-month-old 3xTg mouse, but the numbers of single dots and their clusters are considerably enhanced as h also shows for Reelin-ir. i Vascular AQP4-ir appears very strong in the fissura hippocampalis. j The merged staining patterns demonstrate that all dots in the frequently occurring clusters are co-labelled for SP-C and Reelin. Bars: a,b = 500 μ m, e,i= 200 μ m (also valid for c,d,g,h), f,j = 100 μ m.

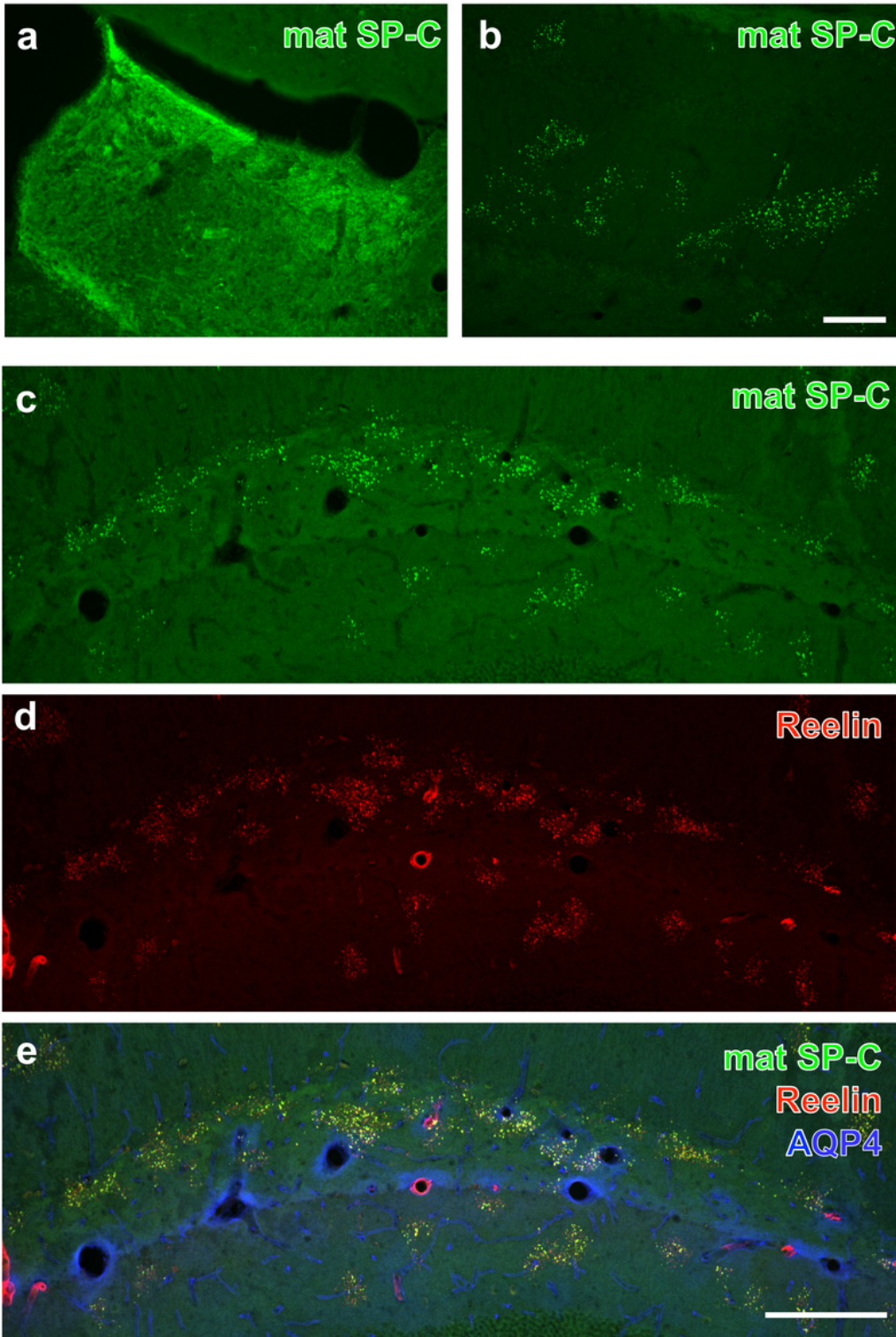


Figure 11

Green fluorescent Cy2-Ir of mature SP-C (mat SP-C) of the habenula (a) and age-dependent clusters of hippocampal dots without counterstaining (b) and in combination with reelin and AQP4-ir (c-e) in a 16-month-old WT mouse (a,c-e) and in an age-matched 3xTg mouse (b). a The medial habenula shows immunoreactivity for mature SP-C. b Clusters of mat SP-C dots are especially dominant in the fissura hippocampalis. c Extended clusters of dots are found in the stratum radiatum, stratum oriens and fissura

hippocampalis. d Reelin-Ir of the dots. e In the merged staining patterns yellowish appearing structures double-labelled by mat SP-C and Reelin as well as some red dots showing only Reelin could be detected. Additionally visible is the vascular labelling with AQP-4-Ir (colour-coded in blue), which appears strongest in the hippocampal fissure. Bars: b = 100 μ m (also applies to a), e = 200 μ m (also applies to c,d).

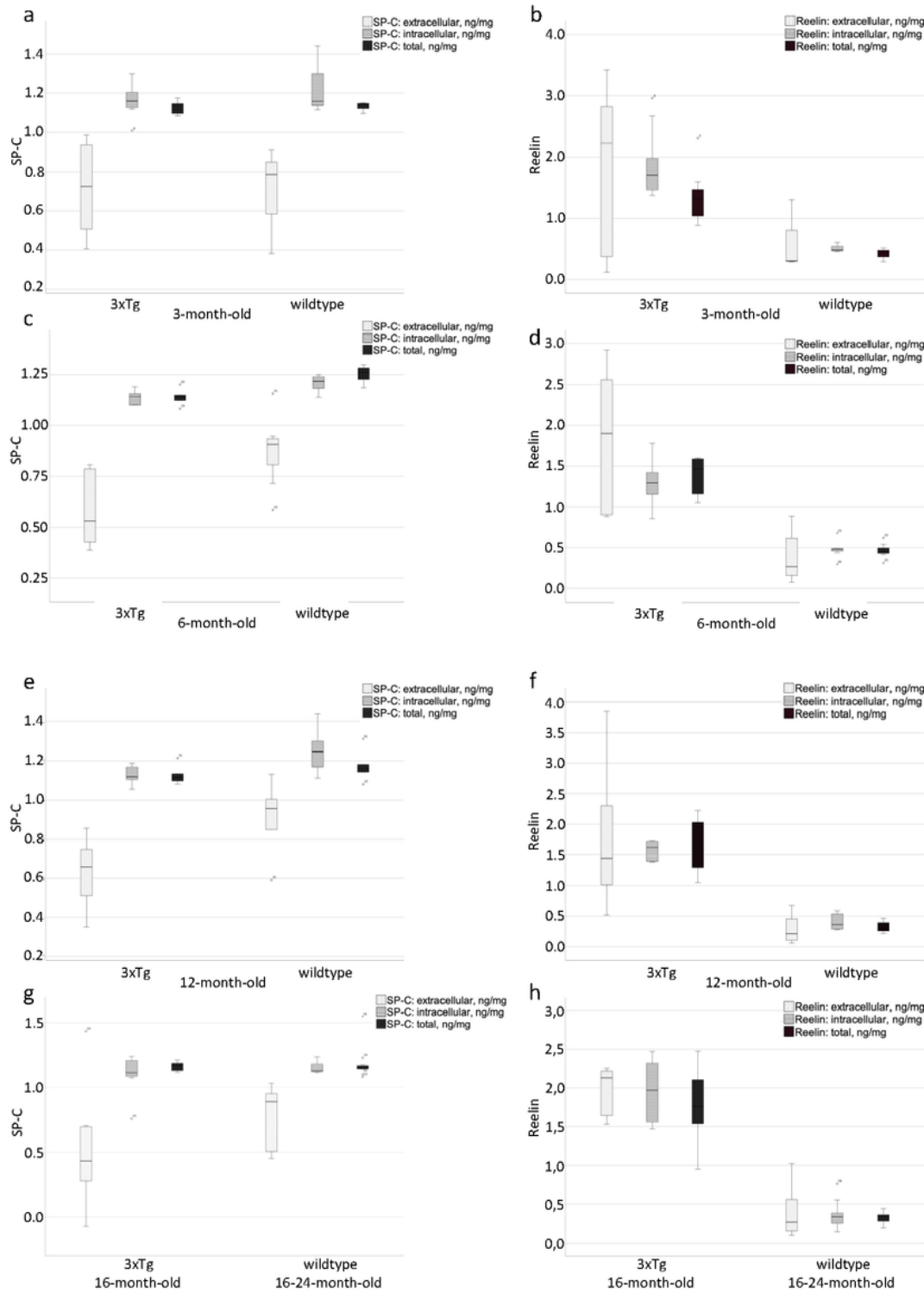


Figure 12

Comparison of SP-C and Reelin between 3x-Tg and WT mice of different ages. Grouped boxplots (a,b) comparing SP-C and Reelin from the extracellular compartment, the intracellular compartment and the total amount between 3xTg and WT mice at the age of 3 months. The differences regarding extracellular Reelin ($p=0.05$), intracellular Reelin ($p=0.01$) and total Reelin ($p=0.01$) are statistically significant. Grouped boxplots (c,d) comparing SP-C and Reelin from the extracellular compartment, the intracellular compartment and the total SP-C and Reelin between triple transgenic and wildtype mice at the age of 6 months. The differences regarding extracellular SP-C ($p=0.013$), intracellular SP-C ($p=0.008$) and total SP-C ($p<0.001$) are statistically significant, as are the differences concerning all Reelin fractions ($p=0.001$ in all instances). Grouped boxplots (e,f) comparing SP-C and Reelin from the extracellular compartment, the intracellular compartment and the total amount of each protein between triple transgenic and WT mice at the age of 12 months. The differences regarding extracellular SP-C ($p=0.023$), intracellular SP-C ($p=0.030$) extracellular Reelin ($p=0.006$), intracellular Reelin ($p=0.004$) and total Reelin ($p=0.004$) were statistically significant. Grouped boxplots (g, h) comparing SP-C and Reelin from the extracellular compartment, the intracellular compartment and the total amount of each protein between triple transgenic and wildtype mice at the age of 16-24 months. A trend of higher extracellular SP-C in the WT animals was observable but did not achieve statistical significance ($p=0.176$). Differences regarding Reelin from all origins were significant (extracellular Reelin: $p<0.001$, intracellular Reelin: $p<0.001$ and total Reelin: $p=0.002$). Concentrations of SP-C and Reelin are expressed in ng / mg total protein. ●: Data value lies between 1.5 and 3x of the interquartile range away from the median value. *: Data value lies >3 times of the interquartile range away from the mean value.

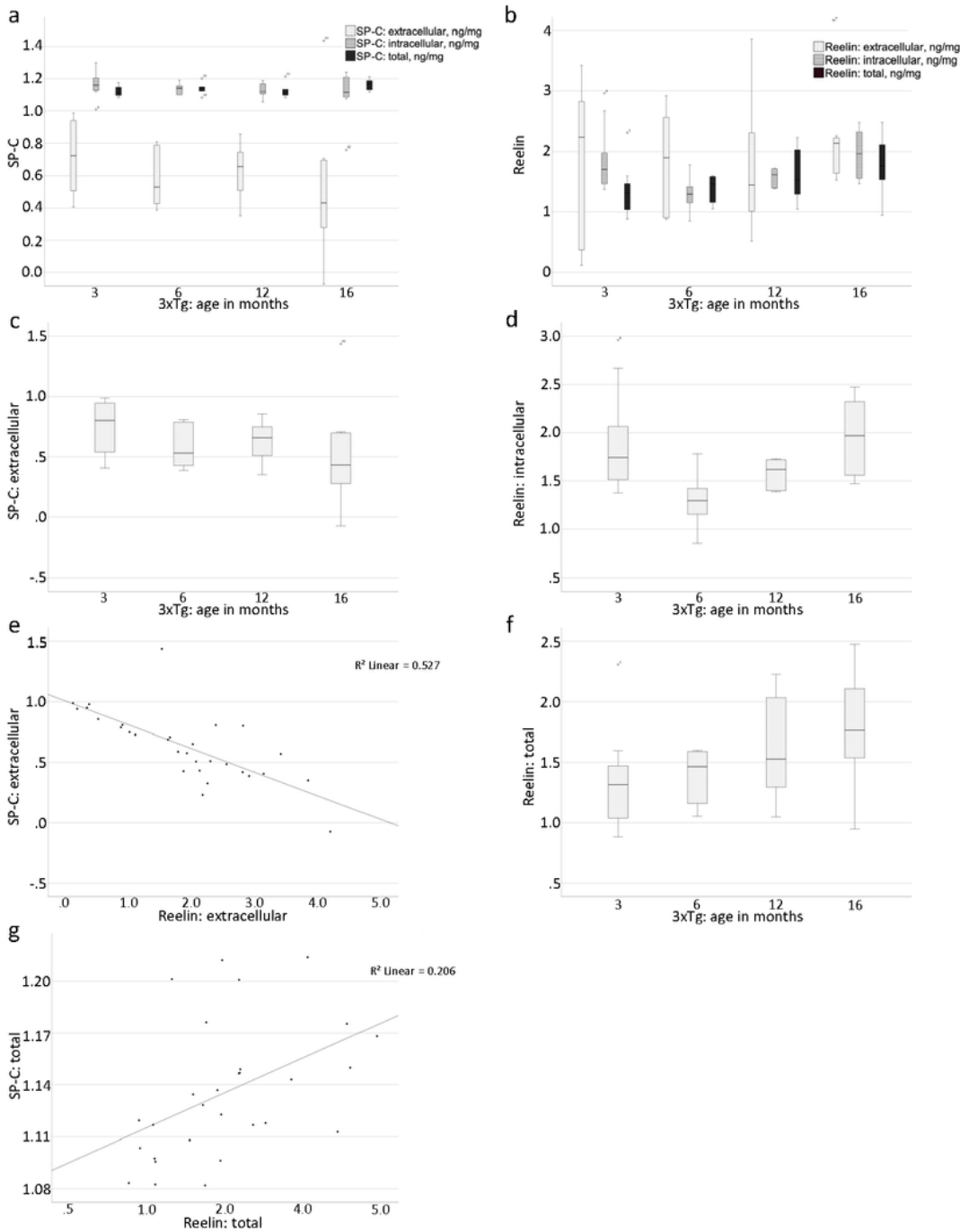


Figure 13

Reelin and SP-C in 3x-Tg mice of different ages. Grouped boxplots (a,b) demonstrate SP-C and Reelin levels from all origins in triple transgenic animals of different ages. The differences regarding intracellular Reelin (d; $p=0.019$) and total Reelin (f; $p=0.022$) were statistically significant, illustrated by the respective unidimensional boxplots. The trend of extracellular SP-C (c) did not reach statistical significance ($p=0.076$). The scatterplot in (e) demonstrates the relationship between extracellular SP-C

and extracellular Reelin ($r=-0.780$, $p<0.001$). The scatterplot in (g) illustrates the statistically significant relationship between total SP-C and total Reelin ($r=0.540$, $p=0.002$). Concentrations of SP-C and Reelin are expressed in ng / mg total protein. ●: Data value lies between 1.5 and 3x of the interquartile range away from the median value. *: Data value lies >3 times of the interquartile range away from the mean value.

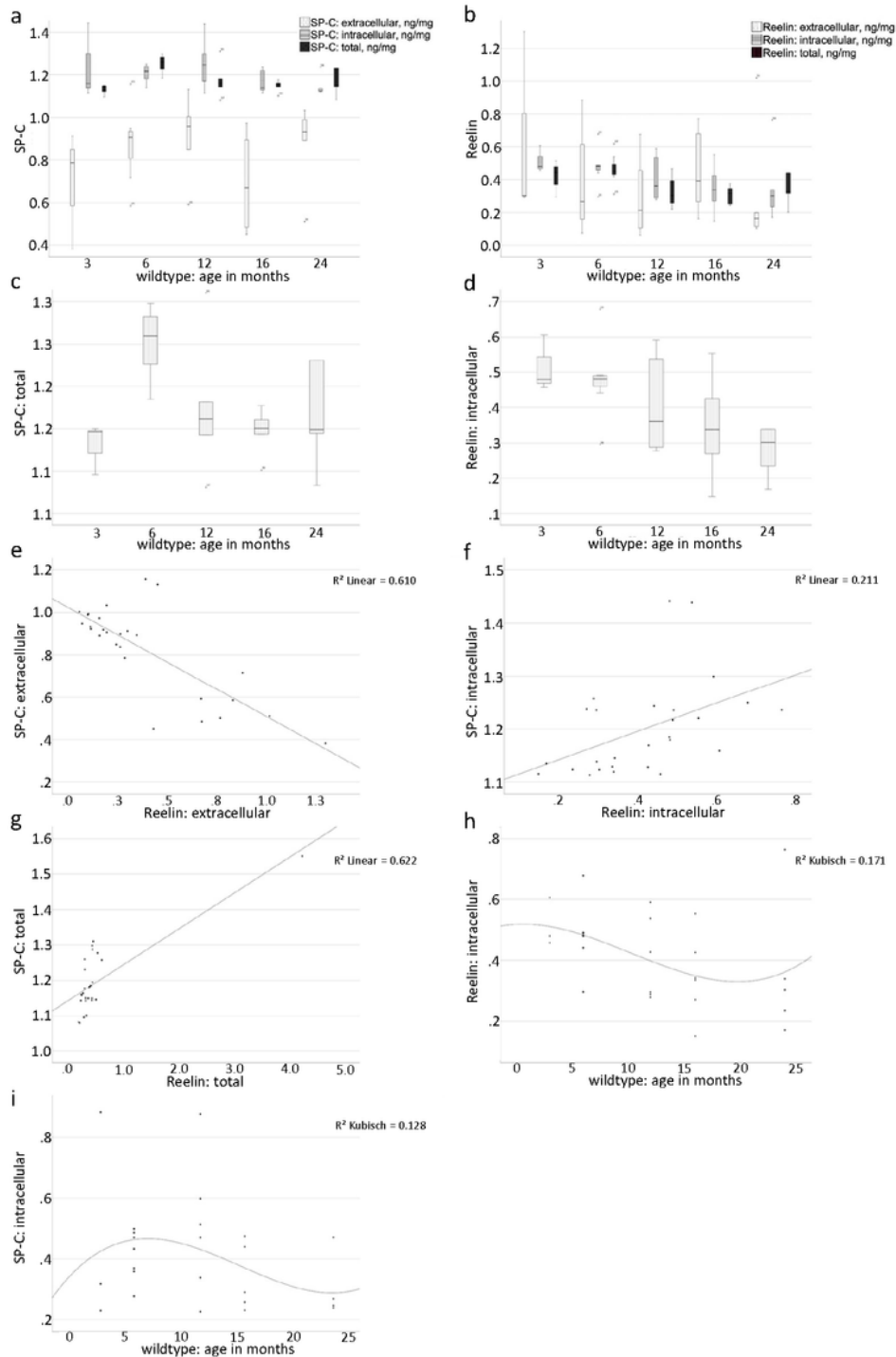


Figure 14

Reelin and SP-C in WT mice of different ages. Grouped boxplots (a,b) demonstrate SP-C and Reelin levels from all origins in wildtype animals of different ages. The differences regarding total SP-C (c;p=0.037) and intracellular Reelin (d;p=0.020) were statistically significant, illustrated by the respective unidimensional boxplots. The scatterplot in (e) demonstrates the statistically significant relationship between extracellular SP-C and extracellular Reelin ($r=-0.780$, $p<0.001$). The scatterplot in (f) shows the significant relationship between intracellular SP-C and intracellular Reelin ($r=0.510$, $p=0.007$). The scatterplot in (g) illustrates the statistically significant relationships between total SP-C and total Reelin ($r=0.540$, $p=0.002$). The correlation between intracellular Reelin and age ($r= -0.444$, $p=0.020$) is shown in (h), whereas (i) demonstrates the statistically significant relationship between intracellular SP-C and age ($r=-0.325$ $p=0.098$). Concentrations of SP-C and Reelin are expressed in ng / mg total protein. ●: Data value lies between 1.5 and 3x of the interquartile range away from the median value. *: Data value lies >3 times of the interquartile range away from the mean value.

Supplementary Files

This is a list of supplementary files associated with this preprint. Click to download.

- [Table3.docx](#)